Click here to access/download;Manuscript (non-LaTeX);Huang_Decay_JAS2026_v2_edit6.docx

What Cause the Decay of Supercell Tornadoes: The Critical Importance of Maintaining Very Low-level Mesocyclone overhead

Wei Huang[a] and Ming Xue[b]

[a]*Key Laboratory of Mesoscale Severe Weather/Ministry of Education, School of Atmospheric Sciences, Nanjing University, Nanjing, Jiangsu 210023, China*

[b] *Center for Analysis and Prediction of Storms and School of Meteorology, University of Oklahoma, Norman, OK 73072, USA*

Submitted to J. Atmospheric Science

July 10, 2026

Corresponding author

Ming Xue, mxue@ou.edu

ABSTRACT

An idealized supercell simulation is conducted using a horizontal grid spacing of 50 m with surface drag representative of land surfaces. Four tornadoes develop sequentially in the simulation. Focusing on the strongest, third tornado, we investigate the processes governing tornado decay. The results indicate that vertical alignment between the tornado and the mesocyclone at 750–1000 m, hereafter termed the very low-level mesocyclone (VLLM), is critical for tornado maintenance. The tornado weakening coincides with the northward movement of VLLM relative to the tornado. The northward movement of VLLM is generated by the drift of mesocyclones above. The displacement between VLLM and tornado leads to the weakening of dynamic vertical perturbation pressure gradient force (DVPPGF) beneath it, causing the weakening of updrafts and an intensification of downdrafts especially below 500 m. The weakened near-surface updraft reduces vertical stretching and initiates tornado decay.

The northward movement of VLLM on one hand weakens/removes the dynamic-PGF support for the tornado, while also simultaneously deprives the mesocyclones themselves of the upward supply of large vertical vorticity from below. Trajectory analyses and Eulerian vertical-vorticity-budget diagnostics focused on mesocyclones demonstrate that the decrease in low-level updrafts and therefore weakening of upward vertical advection of near-surface vertical vorticity is the primary cause for mesocyclones weakening. The weakened mesocyclones further diminish the DVPPGF that supports the low-level updraft ultimately leads to tornado decay. These results reveal a two-way interaction in which the mesocyclones dynamically support the tornado, while the tornado supplies vertical vorticity needed to maintain the mesocyclones.

SIGNIFICANCE STATEMENT

Tornado decay has received considerably less attention than tornadogenesis. This study shows that maintaining vertical alignment between a tornado and mesocyclone at very low levels (<1 km; VLLM) is critical for tornado maintenance. When the VLLM shifts away from the tornado, dynamic forcing that supports near-surface updrafts weakens, reducing vertical stretching and causing tornado decay. Upward transport of

large near-surface vertical vorticity is also reduced as a result, causing the mesocyclones above to weaken further. There exist two-way interactions: mesocyclones dynamically support the tornado, while the tornado supplies vertical vorticity that helps maintain the mesocyclones. The importance of vertical advection of tornadic vorticity to mesocyclone maintenance has not been noted much before.

1. Introduction

Due to the significant societal impacts of tornadoes, research on tornado dynamics has continued to grow. Many studies have focused on understanding tornadogenesis, particularly the development of pre-tornadic near-surface vertical vorticity (Davies-Jones and Brooks 1993; Davies-Jones 2008; Dahl et al. 2014; Schenkman et al. 2014; Dahl 2015; Markowski 2016; Roberts et al. 2016; Rotunno et al. 2017; Roberts et al. 2020; Tao and Tamura 2020; Markowski 2024). Two primary pathways have been proposed for generating rotation near the surface. One involves tilting baroclinically-generated horizontal vorticity into the vertical direction within storm downdrafts (Davies-Jones and Brooks 1993; Dahl et al. 2014; Markowski and Richardson 2014). The other involves tilting primarily surface-friction-generated horizontal vorticity into the vertical direction by updrafts (Schenkman et al. 2014; Xu et al. 2015; Markowski 2016; Roberts et al. 2016; Roberts and Xue 2017; Yokota et al. 2018; Tao and Tamura 2020). More recently, Markowski (2024) also suggests that significant near-surface vertical vorticity within a turbulent inflow environment can organize and serve as a near-ground rotation source for tornadogenesis.

A key final step in tornadogenesis is the contraction of near-ground rotation into a tornado strength vortex. This contraction is associated with strong low-level updrafts and large vertical acceleration near the surface, which produce strong vertical stretching and intensify vertical vorticity (Parker 2023; Huang and Xue 2025). Because tornado maintenance also requires continued vertical stretching and sustained vorticity supply near the surface, the processes that enable tornadogenesis may also control whether a tornado persists or decays. However, relatively few studies have focused on tornado decay with detailed physical analyses.

Given the central role of vertical stretching in tornado intensification and maintenance, the relative position between the tornado and the updraft that provides stretching can strongly influence whether the tornado persists or decays. In idealized simulations with 100 m horizontal grid spacing, Fischer and Dahl (2022) found that a tornado-like vortex dissipates earlier in simulations with stronger near-ground easterly storm-relative flow, which increases the displacement of the near ground vortex from the main updraft.

Observational studies also indicate the importance of tornado-updraft alignment. Using Verification of the Origins of Rotation in Tornadoes Experiment (VORTEX)

observations, Dowell and Bluestein (2002a,b) found that a mismatch between tornado motion and the motion of the main storm-scale updraft can be associated with tornado decay. In their study, tornado motion was influenced by repeated storm-scale surges of outflow in the rear flank downdraft (RFD) region. Lee et al. (2012) similarly suggested that surging RFD outflow can displace the tornado relative to the storm updraft. In addition to changing the relative position between tornado and updraft, they argued that cold pool air associated with surging outflow can replace more buoyant air surrounding the tornado, thereby promoting decay. Related behavior, in which tornado weakening begins as the circulation becomes wrapped by surging outflow along the rear flank gust front (RFGF), has also been documented in other studies (Wurman et al. 2010; Marquis et al. 2012; French et al. 2014).

In addition to negatively buoyant RFD outflow, previous work has identified a dynamically driven downdraft that can develop during tornado decay. Klemp and Rotunno (1983) described an "occlusion downdraft" located immediately behind the RFGF at low levels and near the center of the low-level circulation. The occlusion downdraft forms when low-level cyclonic vorticity increases rapidly and exceeds those above, so that larger negative perturbation pressure develops near ground, creating downward dynamic pressure gradient force (PGF) that drives the downdraft. Klemp (1987) proposed that tornado decay is closely associated with the development of this occlusion downdraft, although no detailed dynamic analysis was provided at the time. In an idealized simulation with 500 m horizontal grid spacing, Adlerman et al. (1999) showed that as the occlusion downdraft develops, it can interact with the RFD to produce a new convergence zone, initiate a new updraft on the downshear flank, and produce a two-celled updraft structure. It was also *suggested* that the occlusion downdraft can cut off conditionally unstable inflow feeding the upshear updraft, weakening the upshear circulation that supports the tornado. These processes were suggested mainly based on visual examinations of the sequence of events without detailed quantitative analyses in either Eulerian or Lagrangian framework.

More recent high-resolution simulations have reported similar downdraft structures near the tornado during decay. In an idealized simulation with 30 m grid spacing by Orf et al. (2017), a strong downdraft encircling the tornado was found near 1000 m above ground level (AGL) during tornado weakening. Yao et al. (2019) also documented the development of downdrafts over near-surface vorticity beneath the mid-level

mesocyclone during tornado decay in a simulation using a real tornado-case sounding. They suggested that such downdrafts can reduce vertical stretching and contribute to tornado decay. However, neither study provided detailed diagnostics of downdraft formation or clarified the tornado-scale mechanisms by which the downdrafts influence tornado decay. Another common pathway that a tornado decays is to go through the multi-vortex stage of tornado development that involves the development of downdrafts inside the tornado vortex. Typically, at the later stage of tornado development, the maximum vertical vorticity is concentrated into a ring instead of at the center of tornado vortex, with updrafts found along the outer edge of the vorticity ring and downdrafts found inside the ring. Such structures are found in the real-data simulations of several supercell tornadoes (Xue et al. 2014; Mashiko and Niino 2017; Sun et al. 2019; Li and Xue 2026). The vortex ring is often barotropically unstable, causing multiple sub-vortices to develop in the form of nonlinearly amplified unstable vortex Rossby waves (Huang and Xue 2023). Most times, multi-vortex tornadoes subsequently decay (Xue et al. 2014; Sun et al. 2019; Li and Xue 2026), although re-intensification may also occur by regaining one-cell-like vortex structure promoted by increased low-level convergence and vertical stretching along the vortex axis.

Many studies cited above were conducted in the context of cyclic tornadogenesis, in which a supercell produces a sequence of tornadoes over time (Lemon and Doswell 1979; Burgess et al. 1982; Dowell and Bluestein 2002a; Adlerman and Droegemeier 2002, 2005; Beck et al. 2006; French et al. 2008; Lee et al. 2012). Although these studies provided useful evidences on the structure and evolution at the storm and tornado scales during the tornado decay stage, detailed diagnostic analyses of tornado scale mechanisms remain limited (Rasmussen and Straka 2007; Adlerman et al. 1999; Dowell and Bluestein 2002a,b; Beck et al. 2006; French et al. 2008; Lee et al. 2012). Several studies examined storm scale evolution during tornado weakening (Marquis et al. 2012; Houser et al. 2015; Marquis et al. 2016; Orf et al. 2017), but the tornado scale processes responsible for decay were not examined in detail. Rasmussen and Straka (2007) is one of few studies that explicitly examined tornado scale decay processes. They analyzed the evolution of low-level angular momentum and found that during tornado weakening, downward and outward secondary flow outside the tornado funnel transported smaller angular momentum downward, contributing to a broad reduction of

angular momentum and tornado demise. Being based on a single tornado, there is uncertainty with the generality of their findings.

In this study, we quantitively analyze a supercell simulation in which four tornadoes develop and decay in sequence, and try to answer the following questions. What are the key structural changes associated with tornado decay? How does the mesocyclone that provides the essential vertical stretching for the tornado evolve during tornado decay? How do the vertical forcing terms change during the process? What physical processes dominate during tornado weakening?

The remainder of the paper is organized as follows. Section 2 provides an overview of the idealized supercell tornado simulation. The simulation produces a sequence of cyclic tornadogenesis where four tornadoes form one after another. In section 3, the model configurations and the life cycles of the tornadoes are briefly described first. It then focuses on the strongest and longest-lasting third tornado and documents the evolution of the simulated tornado and associated mesocyclones. The relationship between the tornado and the mesocyclones at different height levels, in particular the separation distance between them are carefully examined, and how the related processes affect the maintenance and decay of the low-level tornado are discussed. Section 4 examines the evolution of vertical velocity within the tornado and mesocyclones at different levels, with emphasis on the mesocyclone below 1000 m. It solves for effective buoyancy and diagnoses dynamic pressure perturbations, and examines the associated pressure gradient force and buoyancy force at the tornado vortex scale and the impacts of their changes on tornado decay. Section 5 first investigates the weakening of low-level mesocyclone through diagnostics of the vertical vorticity equation. Trajectory-based parcel analyses are also performed to determine the origins of mesocyclone vorticity during tornado decay. A summary with further discussions are given in section 6.

2. Numerical simulation of the cyclic tornadogenesis

a. The settings of numerical simulation

This study employs the nonhydrostatic Advanced Regional Prediction System (ARPS; Xue et al. 2001) to conduct idealized simulations of supercell tornadoes. The model configuration follows that of Roberts et al. (2016), in which surface drag acts on

both environmental and storm-induced perturbation winds. The simulation domain spans 64 km × 96 km in the horizontal and 16 km in the vertical, with a Rayleigh damping (sponge) layer applied above 12 km AGL. Horizontal grid spacing is 50 m. In the vertical, grid spacing varies from 20 m near the surface to 380 m at the model top, with a total of 80 physical layers. The lower boundary is flat, and the first model level for scalar variables and horizontal momentum is located at 10 m AGL. Radiation open lateral boundary conditions are applied at four lateral boundaries. Fourth-order advection schemes are used in both horizontal and vertical directions while the scalar variables are advected by the monotonic flux-corrected-transport (FCT) scheme. Subgrid-scale (SGS) turbulence is parameterized using the 1.5-order turbulent kinetic energy (TKE) closure scheme mostly following Moeng and Wyngaard (1988), together with a weak fourth-order computational diffusion. The Lin et al. (1983) single-moment microphysics scheme is employed that has five liquid and ice species. The snow and hail intercept parameters use the default values of Lin et al. (1983) as 3×10^6 m^{-4}, and 4×10^4 m^{-4}, respectively. While the intercept parameter for rain drop size distribution is set to 2×10^6 m^{-4} or a factor of 4 smaller than the default values. Such values were also used in Roberts et al. (2016), and the reduced rain intercept parameter implies a smaller number of larger rain drops that results in less evaporative cooling and, weaker and more realistic supercell cold pools, according to Snook and Xue (2008), and Dawson et al. (2010). The model configurations are the same as used by Roberts et al. (2016) except for the use of FCT scheme for scalars here.

The idealized simulation is integrated forward in time for 7200 s in our study. The analyses presented in this study are based on model output with a temporal resolution of 1 second. Because the main purpose of Roberts et al. (2016) is to investigate the effects of surface drag on supercell storm and tornado dynamics. To keep the environmental wind profile away from the convective storm steady in the presence of surface drag, they first performed a "spin-up" simulation for 48-hours, during which the wind profile was allowed to adjust to surface drag while subject to the Coriolis force and a horizontal pressure gradient force (PGF) specified in terms of the background geostrophic wind. The final state is in a geotriptic balance, a balance among the Coriolis force, PGF and the frictional force.

Usually the frictional force is significant only within the planetary boundary layer where momentum fluxes of turbulent motion triggered and supported by thermal and

kinematic instabilities act as frictional momentum stresses on the air parcels. The effect of surface drag is propagated upward through such momentum fluxes while at the ground level, the negative momentum flux or stress is parameterized using a drag law. The drag law calculates the surface stress as a drag coefficient, C_d, multiplied by horizontal wind vector at the lowest model level and the wind speed. This stress is in the opposite direct as the surface wind, although the actual frictional force acting on the air parcel in the first model layer is equal to the difference between the stresses defined at the top and bottom boundaries of the layer, with the bottom boundary located at the ground level.

The spin-up simulation was run using ARPS configured the same as the actual three-dimensional (3D) supercell simulations, except for the horizontal dimension that is assumed uniform. So effectively, the ARPS was run in one-dimensional model, with turbulence mixing acting only in the vertical direction. Therefore, the interior momentum fluxes are all parameterized by the SGS turbulence scheme. The same spin-up procedure was used in Roberts et al. (2016), Roberts and Xue (2017)), and Oliveira et al. (2022), and was discussed intensively in Dawson et al. (2019). This spin-up procedure is actually similar to that used by Markowski (2020), except that he used a 3D large-eddy-resolving simulation (LES) and ran it for 12 hours to obtain a quasi-steady wind profile which also adjusted the temperature and moisture profiles somewhat (see his Figure 1).

The environmental thermodynamic sounding and the wind hodograph used as the initial input for the spin-up run was extracted from a real-data simulation of the 3 May 1999 central Oklahoma tornado outbreak, as described in Dawson et al. (2010). The sounding was extracted from the inflow region of the simulated storm at 2300 UTC or 1700 LST. Roberts et al. (2016) used the original extracted hodograph (MAY3 in their Fig. 1) to define the base-state wind profile for the spin-up simulation, which is effectively assumed to be the background geostrophic wind. In reality, this extracted hodograph has subject to the effect of boundary layer friction therefore assuming the profile is geostrophic at the lower levels is inappropriate. For this study, we modified the original extracted hodograph by setting the wind below 500 m to a constant value of (-11, 11) m s^{-1} (Fig. 1a). This modified hodograph is effectively assumed to be geostrophic during the spin-up simulation. It shares similar characteristics as the starting hodograph of Markowski (2020) that also played the role of background

geostrophic wind profile, in that the wind speed is quite large at the ground level and vertical wind shear below 1 km is small (see blue line in his Fig. 1b). A similar spin-up procedure is also used and discussed in Li and Xue (2026) where the background geostrophic wind profile is estimated from the ERA5 global reanalysis.

After the 48-hour spin-up, the final temperature and moisture profiles and hodograph used to define the background state for the 3D supercell storm simulation with surface drag are shown by the solid lines in Fig. 1. The storm is initialized by introducing an ellipsoidal potential temperature (θ) perturbation centered at x = 40 km, y =56 km, and z = 1.5 km. The θ perturbation has a horizontal radius of 10 km and a vertical radius of 1.5 km, and a maximum perturbation of 6 K at the center following Roberts et al. (2016). To keep the simulated storm near the center of the domain throughout the simulation, the model domain is translated at a constant speed of 9.8 m s^{-1} in the x-direction and 7.8 m s^{-1} in the y-direction, consistent with the observed storm motion estimated by Roberts et al. (2016). Further details regarding the simulation setup can be found in Section 2a of Roberts et al. (2016).

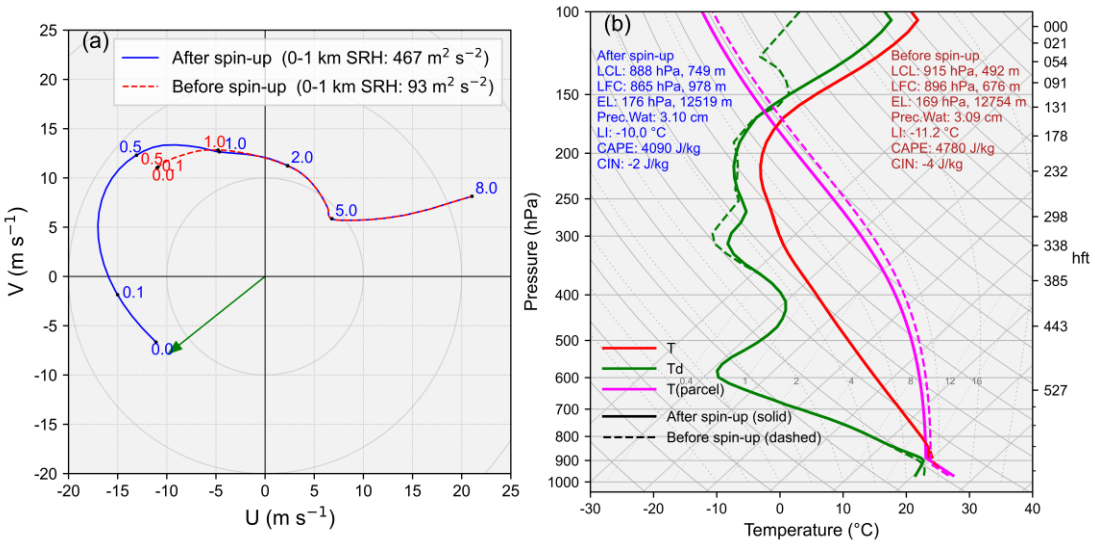


Fig. 1 (a) Wind hodograph for storm-relative soundings showing the modified extracted hodograph, in which winds below 500 m are set to a constant vector (dashed red), and the final hodograph after 48 hours of spin up (solid blue), plotted up to 8 km AGL. Numerical values along the hodograph indicate the height AGL (km) of the nearest black dot. Above 1 km AGL, the two hodographs are qualitatively similar. The green arrow denotes the ground-motion vector added to the extracted wind profile to obtain a quasi-stationary storm in the simulations. The 0–1-km AGL storm-relative helicity is provided for each hodograph in the legend. (b) Skew-T log p diagram for sounding of the original extracted hodograph (dashed lines) and final wind profile 48h (solid lines). The

environmental temperature and mixing ratio are denoted by red and green lines, respectively. The temperature for an ascending surface-based parcel is denoted by the pink line.

b. The overview of the simulated four tornadoes

From 1200 to 7200s, four tornadoes are generated sequentially, i.e., the simulation goes through cyclic tornadogenesis processes (Lemon and Doswell 1979; Burgess et al. 1982), as shown by the time-height plots of domain-wide maximum vertical vorticity (ζ_{max}), maximum vertical velocity (w_{max}), and minimum perturbation pressure (p'_{min}) in Fig. 2. The durations of the four tornadoes are indicated by the four red rectangles in the figure. The first tornado forms quickly, at about 1800 s into the simulation, somewhat later than the ~1500 s obtained in Roberts et al. (2020). The rapid development might have benefited from the rather large 6 K maximum perturbation of the initial thermal bubble that triggered the storm, and in the real world, it would correspond to cases with strong local thermal or dynamic forcing that triggers the convection. Roberts et al. (2016), Roberts and Xue (2017), and Roberts et al. (2020) focused on the tornadogenesis processes of the first tornado in their simulations. Vorticity generated by surface drag on the storm-scale flows was shown to be the primary source of vorticity for both the tornado and the mesocyclone supporting this first tornado.

Among the four simulated tornadoes, the first and third tornadoes are more intense than the other two. The w_{max} of the first and third tornadoes can lower to below 1500 m, and below 200 m in the case of first tornado (Fig. 2b). Such strong updrafts at very low levels correspondingly create very strong vertical stretching and generate large vertical vorticity ζ at the low levels (Fig. 2a). The p'_{min} of first and third tornadoes also reaches lower values (Fig. 2c). The first tornado forms at ~1780 s and ends at ~2300 s and is similar to the study of Roberts et al. (2016). The second tornado lasts from ~ 2900 to 3900 s. The third one forms at ~4050 s and does not completely die until 6800 s. It is also the strongest. During its life cycle, it goes through several phases of weakening and re-intensification. For example, it weakens between ~ 4900 and 5100 s and intensifies again between 5100 and 5400 s. Despite the intensity variations, the near-surface ζ_{max} and maximum wind speed remain greater than 0.2 s^{-1} and 29 m s^{-1}, respectively, satisfying the EF0-scale tornado criteria. The fourth tornado lasts only

from ~ 6700 to 7200 s and is also the weakest. In this paper, we focus our analyses on the decay processes of the third tornado while leaving the cyclic tornadogenesis processes to future investigations.

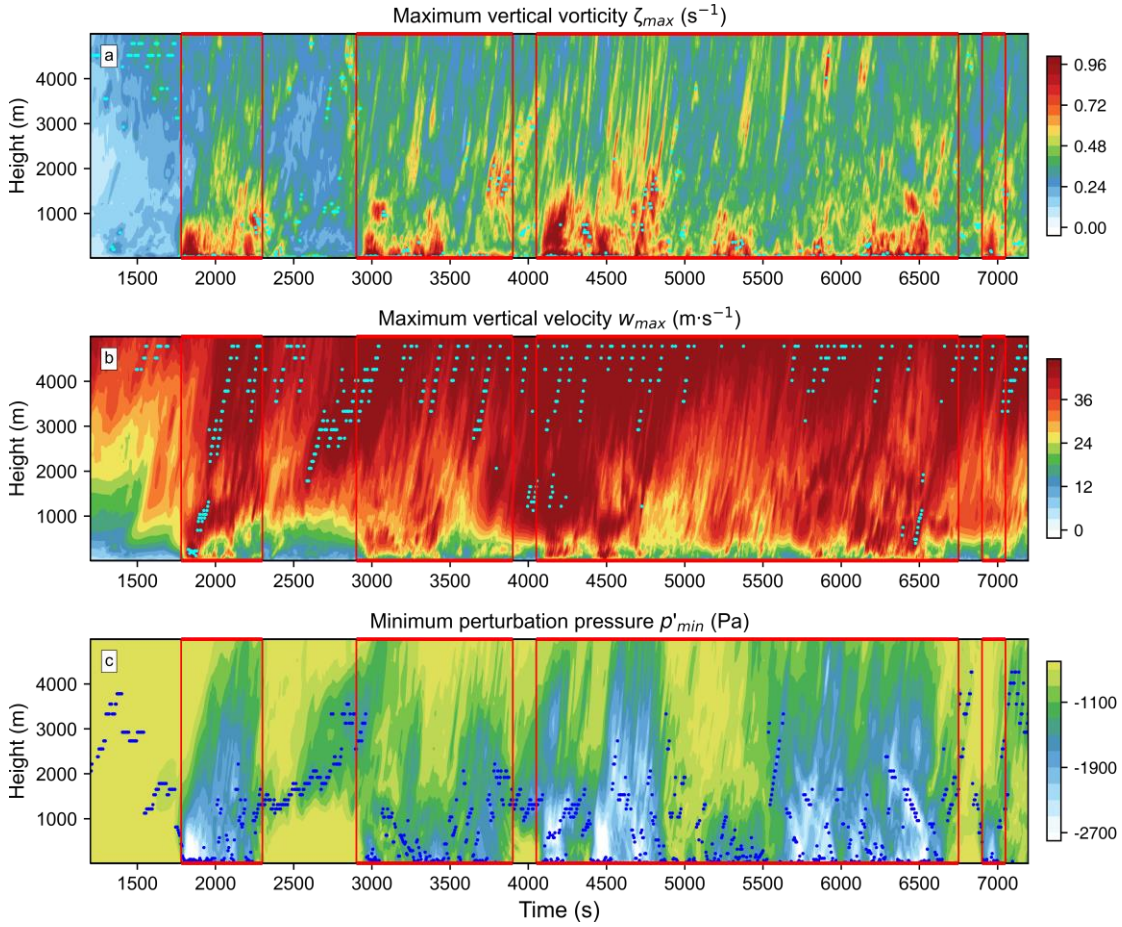


Fig. 2 Time-height section of domain-wide (a) maximum vertical vorticity ζ_{max} (s^{-1}), (b) maximum vertical velocity w_{max} (m s^{-1}), and (c) minimum perturbation pressure p'_{min} (Pa), from 1200 to 7200 s. The time periods of the four tornadoes existed are indicated by four red rectangles. The cyan dots in (a) and (b) and blue dots in (c) denote the height levels of the maximum or minimum values of the corresponding fields at the times.

3. The decay processes of the third tornado

a. Overview of tornado decay

The time that the surface ζ_{max} reaches its maximum is at 6525 s for the third tornado. Therefore, in our study we mainly investigate storm- and tornadic-scale evolutions between 6300 and 6800 s. Fig. 3 presents time–height cross sections of ζ_{max}, w_{max}, w_{min} and p'_{min} from 6300 through 6795 s, over a subdomain with 4 $\times$ 4 km^2 containing the tornado and associated mesocyclones. Due to the tilting with height of

the tornado-mesocyclone vortex (as will be discussed in section 3c), the center of domain used to calculate the extrema is set to the local minimum in p' associated with mesocyclones at different levels. The domain center tilts mostly northward with height during this period. Between 6300 and 6525 s, ζ_{max} below 1000 m intensifies dramatically, with ζ_{max} exceeding 0.5 s^{-1} for the entire depth below 1000 m by 6525 s (Fig. 3a). The intensification of ζ_{max} is associated large w_{max} with the strong updrafts founding extending from below 100 m through 5000 m and above (Fig. 3b). The vertical gradient of w_{max} is greater than 0.16 m s^{-2} below 250 m and actually w_{max} jumps from 0 to about 30 m s^{-1} within the lowest 100 m AGL, indicating extremely strong vertical stretching of ζ during this period. As indicated by the right-ward tilted phase lines (black lines with arrowhead) in the time-height cross sections, both ζ_{max} and w_{max} show upward propagation trend, suggesting upward advection of large ζ that develops and intensifies at near-ground levels. Such upward progression of ζ_{max} and w_{max} has also been documented in previous observational and numerical studies (Houser et al. 2015; Roberts et al. 2016; Bluestein et al. 2019). Corresponding to the intensification of ζ_{max} below 1000 m (Fig. 3a), the height of the smallest (in absolute, negative value) p'_{min} lowers from 1500 m to near-surface between 6400 and 6500 s (Fig. 3d), indicating the rapid lowering of strongest low-level mesocyclone. More accurately, the strongest rotation within the mesocyclone vortex shifts downward.

The ζ_{max} decreases significantly after 6525 s as w_{max} of the updrafts especially that below 500 m weakens (Fig. 3b). The ζ_{max} greater than 0.5 s^{-1} is mainly found below 250 m after this time (Fig. 3a). The corresponding p'_{min} jumps from about -27 to about -12 hPa after 6525 s (Fig. 3d). At the same time, the strongest downdrafts quickly descend from ~2000 m to ~1000 m by 6575 s (green dots in Fig. 3c). The lower edge of $w_{max} \leq$ -32 m s^{-1} has lowered to ~300 m by 6700 s. The above results suggest that the rapid weakening of updrafts below 500 m and rapid descent of the downdraft core, and intensification of downdrafts below 1000 m play important roles in tornado decay. Before the rapid jump in p'_{min} at 6550 s (Fig. 3d), the p'_{min} is strongest at the surface and reaches below – 27 hPa. The associated strong downward PGF most likely plays a significant role in the onset of strong downdrafts. The causes for the intensification of downdraft and weakening of updrafts during this period will be examined quantitatively later in section 4b.

We also note that between 6600 and 6650 s, ζ_{max} below 1000 m briefly reintensifies (Fig. 3a) and the surface p'_{min} lowers to -19 hPa at the same time (Fig. 3d). These are accompanied by a brief reintensification of updrafts below 500 m (Fig. 3b). All three quantities rapidly weaken afterwards almost simultaneously.

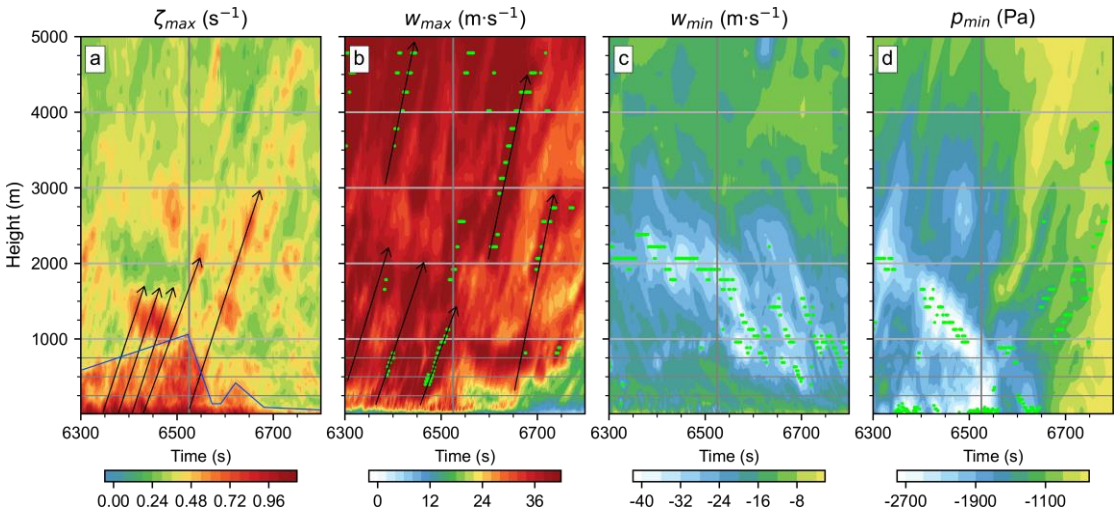


Fig. 3 Time-height sections of horizontal subdomain-wide extrema (a) ζ_{max} (s^{-1}), (b) w_{max} (m s^{-1}), (c) w_{min} (m s^{-1}), and (d) p'_{min} (Pa), valid from 6300 to 6795 s. The green dots in (b–d) denote the height levels of the extreme values of the corresponding fields at the times. The green dots are not shown in (a), because ζ_{max} is always located at the lowest scalar level (10 m) during the period shown. The vertical gray lines are the time that the surface ζ_{max} reaches its maximum at 6525 s. The horizontal gray lines are drawn at 250, 500, 750, 1000, 2000, 4000 m AGL. The black line in (a) and (b) denote the upward propagating trend of ζ_{max} and w_{max}. To better show the intensity change of ζ_{max}, the approximate trend of ζ_{max} below 1000 m is represented by blue line segments.

b. Low-level structures through tornado decay

At 6315 s, the tornado vortex consisting of three subvortices is located at the intersection of the forward-flank gust front (FFGF) and the primary rear-flank gust front (PRFGF) (red solid lines in Fig. 4a). Strong convergence is the most prominent feature along these gust fronts. Another zone with pronounced convergence exists west of the PRFGF, which is the secondary rear-flank gust front (SRFGF; dashed red line in Fig. 4a) described in previous studies (Mashiko et al. 2009; Wurman et al. 2010; Lee et al. 2012; Marquis et al. 2012; Kosiba et al. 2013; Schenkman et al. 2014; Skinner et al. 2014). Strong potential temperature (θ) gradient is evident across the FFGF and across the portion of SRFGF close to tornado. While the PRFGF is located within a zone of positive θ perturbations (θ') with weak gradient (Fig. 4a). This relatively warm air

originates from repeated surges of warm air generated within the rear-flank downdraft (RFD) region prior to 6315 s (not shown). After 6315 s, the SRFGF with the cold air behind with $\theta' <$ -5 K and strong northerly winds, advances southward and eastward (Fig. 4b–d). Before 6525 s, the tornado locates at the triple point among RFGF, FFGF, and SRFGF. By 6600 s, the SRFGF has caught up with the PRFGF (Fig. 4e) so that the tornado becomes fully wrapped in cold air and starts to weaken (Fig. 4e). As the cold air continues to propagate northward, the FFGF becomes indistinct by 6625 s (Fig. 4f). In the subsequent few minutes, the RFGF near the tornado also disappears as cold air spreads and fills up all quadrants around the tornado. The southern portion of the RFGF remains to the southeast of the tornado as the cold air pushes further southeastward behind the remaining warm air (Fig. 4g–h).

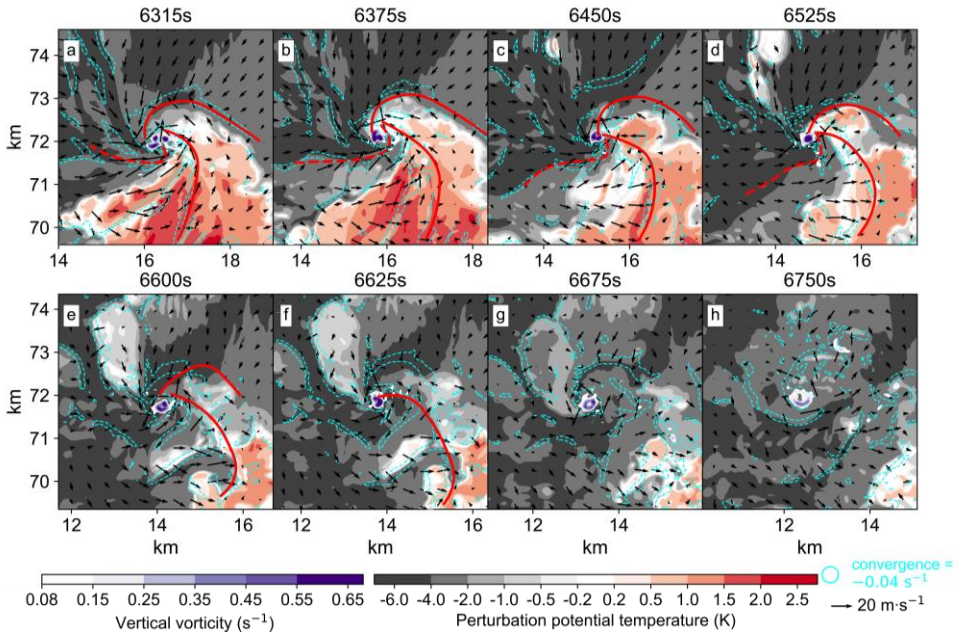


Fig. 4 Horizontal cross sections of perturbation potential temperature, θ' (gray-to-red shaded; K), ζ (purple shaded; m s^{-1}), convergence (cyan dashed contours at -0.04 s^{-1}), and ground-relative wind (vectors; m s^{-1}) at 10 m AGL at (a) 6315, (b) 6375, (c) 6450, (d) 6525, (e) 6600, (f) 6625, (g) 6675, and (h) 6750 s. The positions of FFGF and PRFGF are indicated by red solid lines, while the position of SRFGF is indicated by red dashed line.

A zoomed-in view of the region surrounding the tornado is presented in Fig. 5. As mentioned earlier, at 6315 s, the tornado exhibits a multiple sub-vortex structure (Fig. 5a), a structure that often develops in the later life cycle of tornadoes (Fujita 1970, 1972; Rotunno 1984; Lewellen et al. 1997; Fiedler 1998; Wurman 2002; Kosiba and Wurman 2010; Xue et al. 2014; Nolan et al. 2017; Mashiko and Niino 2017; Yao et al. 2019;

Huang and Xue 2023) and has been shown to be due to barotropic instability of the tornado vortex after its near-surface vorticity gains a vortex ring structure (Huang and Xue 2023). In this relatively long-lived tornado, the multivortex structure is present from 5400 s (not shown) through 6450 s (Fig. 5c). Between 6315 and 6525 s, the overall tornado vortex shrinks in diameter, and the three sub-vortices converge, reestablishing a single maximum vorticity core by 6525 s (Fig. 5d). The single-core structure corresponds to the one-cell tornado structure, in which the ζ_{max} is located at the tornado vortex center (Fig. 5d; Davies-Jones et al. 2001). At this time, the tornado is both most axisymmetric and strongest (Fig. 5d). After 6525 s, the tornado vortex again transitions back to a vorticity ring structure with two to three sub-vortices (Fig. 5e–g). Though the vortex reintensifies slightly around 6625 s (Fig. 5f), the vortex again weakens and expands in diameter after 6625 s (Fig. 5g and h).

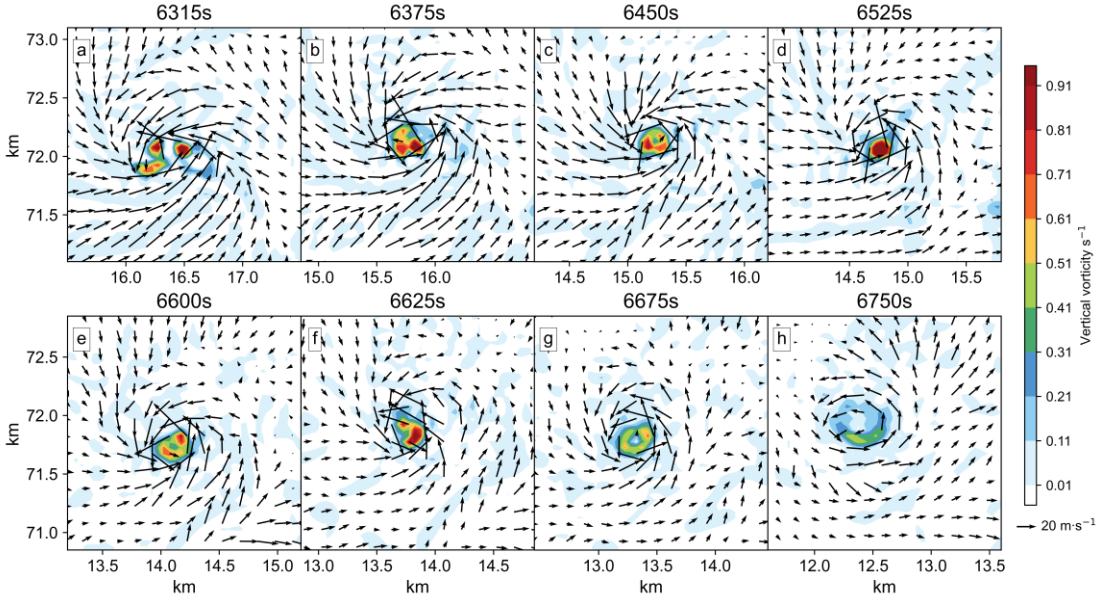


Fig. 5 Horizontal cross sections of ζ (shade; s^{-1}) and ground-relative wind (vectors; m s^{-1}) at 10 m AGL at (a) 6315, (b) 6375, (c) 6450, (d) 6525, (e) 6600, (f) 6625, (g) 6675, and (h) 6750 s.

c. The evolution of overlying mesocyclones

In section 3a, we have shown that the weakening of updrafts and intensification of downdrafts are closely associated with tornado decay. The intensity of updraft is directly modulated by mesocyclones. To investigate the processes that may have caused the weakening of the low-level updrafts and, consequently, the tornado, we further examine the evolution of the mesocyclones overlying the tornado vortex. Fig. 6 presents

three-dimensional visualization of ζ isosurfaces. At 6315 s, the 0.18 s^{-1} ζ isosurface forms a nearly continuous column from the surface to about 4000 m, with significant tilting of the vortex tube above 1000 m (Fig. 6a). Although the surface maximum ζ continues to increase substantially between 6315 and 6525 s, weakening of low-level mesocyclone starts before 6375 s, with the 0.18 s^{-1} ζ isosurface becoming discontinuous at around 2000 m (Fig. 6b). Therefore, the weakening of low-level mesocyclone proceeds the maximum surface vortex intensity at around 6525 s (Fig. 5d). As time progresses, the vertical gap between mid-level and low-level mesocyclones with ζ exceeding 0.18 s^{-1} expands, while the horizontal separation between the mesocyclones at the two levels also increases somewhat (Fig. 6c). Similar weakening of mesocyclone between ~1500 to 2000 m prior to tornado dissipation was observed by French et al. (2014) and Houser et al. (2015) in Doppler radar observations.

By 6525 s, an additional discontinuity develops in the mesocyclone vortex tube near 1000 m (Fig. 6d). The vortex column connected to the surface tornado vortex further contracts vertically, reaching a depth of only ~ to about 750 m by 6600 s (Fig. 6e). The mesocyclones between 750 and 1000 m weakens substantially between 6525 and 6675 s (Fig. 6f). Following the progressive weakening of the mesocyclone at increasingly lower levels, the surface tornado vortex starts to weaken rapidly after 6525 s (Fig. 5d-h). This sequence of events suggests that the weakening of low-level mesocyclone is the direct cause of tornado weakening in this case.

We also note that although the weakening of mesocyclones near 2000 m is observed first, the mesocyclones above 2000 m are not dissipated immediately. Upward vertical advection of vertical vorticity from lower levels appears to help maintain the mesocyclones at these heights, as shown in the supplementary animation of vertical vorticity. However, after 6525 s, as the tornado begins to decay, the mesocyclones can no longer be maintained and also weaken. This behavior suggests that mesocyclone maintenance may also be influenced by the surface tornado vortex. Thus, the relationship between the mesocyclone and tornado may be bidirectional.

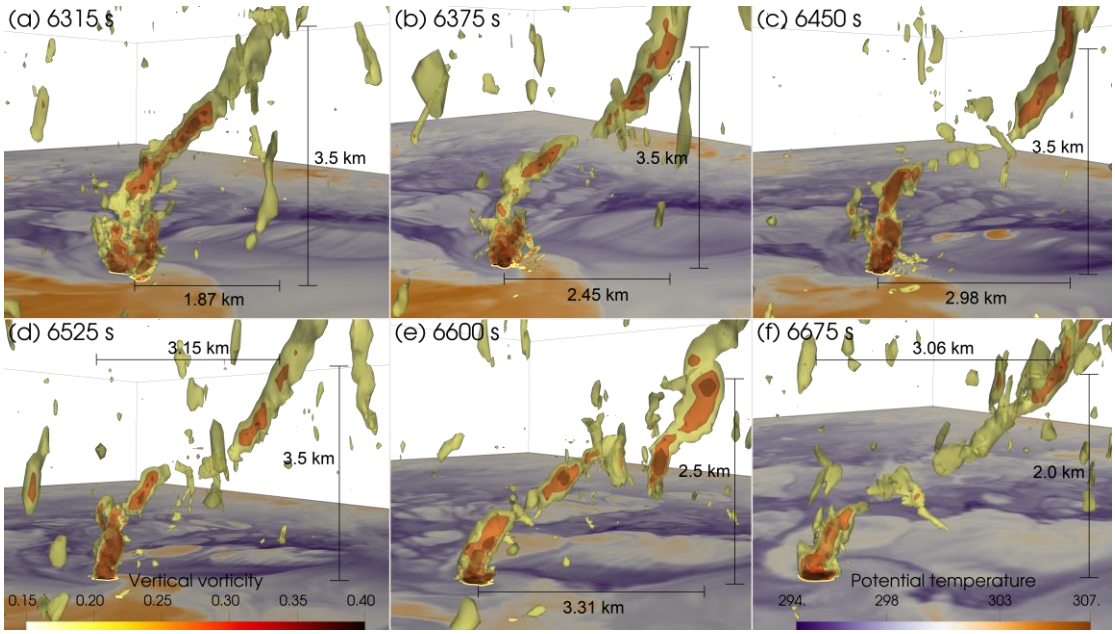


Fig. 6 (a–f) Vertical vorticity ζ (isosurfaces at 0.18, 0.3 0.4 s^{-1}), surface potential temperature (shaded; K), and surface ζ (yellow contours at 0.18 s^{-1}). View is toward the northwest. The vertical and horizontal black lines in each panel indicate the scale height and horizontal extent of the tornado, respectively.

The weakening of low-level mesocyclone appears closely linked to the northward displacement of the overlying (3-4 km AGL) mid-level mesocyclone. At 6315 s, the horizontal distance between surface tornado and the mesocyclone at 3500 m is about 1.8 km (Fig. 6a). The distance increases to ~2.45 km by 6375 s as the mid-level mesocyclone moves northward and a gap in the vertical vortex tube appears at ~2000 m (Fig. 6b). The northward movement of the mid-level mesocyclone appears to drag the mesocyclones below it northward also (Fig. 6c–f), increasing the vertical gap of vortex tube. By 6600 s, the low-level mesocyclone between 0.75 and 2.5 km levels has also drifted northward noticeably and become disconnected with the tornado vortex below (Fig. 6e).

Therefore, there is a downward progression of the northward displacement of the mesocyclones at difference levels, leading to the disconnect among the mesocyclone vortices at these levels. To better illustrate such processes, we calculate the horizontal distances between the surface tornado vortex and mesocyclones at different heights and show the time series in Fig. 7. Between 6200 and 6300 s, the overall tornado-mesocyclone vortex already exhibits a slight northward tilt. The horizontal distance between the tornado and the mesocyclones generally increases with height. The largest displacement, approximately 2.2 km, occurs between the tornado and the mesocyclone

at 4235 m, whereas the smallest displacement, approximately 0.5 km, occurs for the mesocyclone below 1 km, although some temporal fluctuations are present. During this period, the displacements between the tornado and the mesocyclones at all levels remain relatively steady. This persistence indicates that the tornado and the overlying mesocyclones are vertically well aligned during this period, as also seen in Fig. 6a.

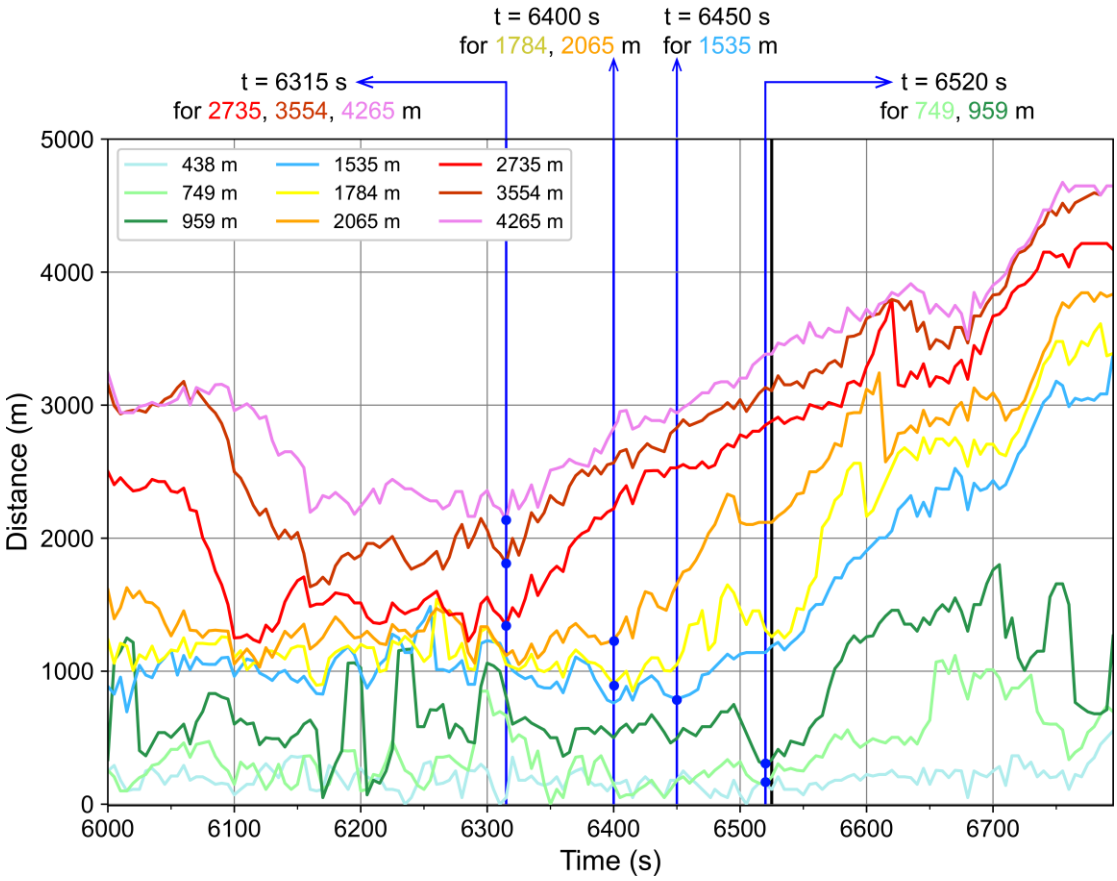


Fig. 7 Time series of the horizontal distance between the surface tornado and mesocyclones at different levels. Colors indicate mesocyclone height. Four vertical blue lines mark the times when the distances begin to increase at various levels. The leftmost blue line at 6315 s marks the time that the distances between surface tornado and mesocyclone at 2735 (red), 3554 (brown), and 4265 (purple) m start to increase. The second blue line at 6400 s corresponds to increases at 1784 (yellow) and 2065 m (orange) increases. The third blue line at 6450 s indicates an increase at 1535 m (azure). The rightmost blue line at 6520 s marks separation from mesocyclones at 749 (slight green) and 959 m (dark green). For, clarity, the times that the distance between mesocyclones and tornado starts to increase are denoted by blue dots. A vertical black line at 6525 s denotes the time when the surface ζ_{max} begins to weaken. The distance between the tornado and the mesocyclone at 438 m (light blue) does not exhibit a clear increase.

At 6315 s, northward displacement of mesocyclones at 2735, 3554, and 4265 m start simultaneously (Fig. 7). This displacement is followed by that of the mesocyclones at

1784 m and 2065 m, which begin their movement at ~6400 s. Shortly before the surface tornado starts to weaken, the mesocyclones at 959 and 749 m also start to drift away from the tornado at ~6520 s. The displacement of the mesocyclone at 959 m proceeds much more rapidly, whereas the northward movement of the mesocyclone at 749 m accelerates markedly near 6650 s. Overall, these results indicate a clear downward progression of northward displacement away from the surface tornado through the mesocyclones at successively lower levels. This temporal sequence suggests that the displacement of the higher-level mesocyclones contributes to the subsequent weakening of the surface tornado.

Marquis et al. (2016) also found that the mesocyclone in a real supercell case was most tilted during the weakening phase of tornado. Similarly, French et al. (2014) found an inverse relationship between tornado vortex signature (TVS) inclination angle and tornado intensity in two observed tornadoes. Together, these results suggest that while some tilting is permissible and even common, excessive tilting is harmful for sustaining a tornado. In our simulation, the increased tilt starts from the mid-level mesocyclones above ~2.7 km. The displacement aloft then induces displacement at lower levels, gradually reducing the depth over which the mesocyclone remains closely aligned with the tornado. The onset of tornado weakening at ~6520 s coincides with the separation of the mesocyclones below 1 km from the surface tornado (Fig. 7). Bluestein et al. (2026) in a study of a cyclonic tornado spawned by the Selden, Kansas, supercell also observed that the vortex tilt is minimized when TVS intensity peaks, increases as the TVS weakens, and eventually reverses its tilt direction during TVS dissipation. However, they only hypothesized that vortex tilt is caused by rear-flank internal surges or from rotation about a nearby larger-scale vortex, without further analysis.

The northward displacement occurs sequentially within three layers; at the mid-levels above 2.7 km, the lower levels between 1 km and 2.7 km, and the levels below ~1 km. Motivated by this grouping, and somewhat consistent with Coffer et al. (2023) who proposed that the low-level mesocyclone near the cloud base is distinct from the midlevel mesocyclone, we adopt distinct terminology for mesocyclones at different levels for clarity in the rest of this paper. Hereafter, we refer to the mesocyclone circulations between 3 and 6 km, between 1 and 3 km, and between 0.75 and 1 km as the mid-level mesocyclone (MLM), low-level mesocyclone (LLM), and very low-level mesocyclone (VLLM), respectively.

We believe that the VLLM is most directly connected to the near-surface tornado vortex; therefore, its intensification, maintenance, and weakening are closely related to the genesis, maintenance and decay of tornado. Our results suggest that the maintenance of a strong VLLM vertically aligned with the tornado vortex depends on the presence of sufficiently strong and well-aligned LLM and MLM circulations above. In the absence of such support, the downward-directed dynamic PGF between the VLLM and the tornado may weaken both circulations (Huang and Xue 2025). Conversely, a strong overlying LLM may reduce this downward-directed forcing at the VLLM level. The effects of the dynamic PGF are quantified in the following section.

4. Vertical acceleration associated with tornado decay

In the previous section, we see that as the VLLM weakens, the associated updrafts, particularly those below 500 m, and the accompanying vertical stretching also weakens, leading to tornado decay. In this section, we examine the evolution of vertical velocity, and identify the dominant forcing terms responsible for the observed changes in vertical motion, with particular emphasis on the period of VLLM weakening.

a. The evolution of vertical velocity

Fig. 8 shows the horizontal cross sections of w at 3125, 1525 and 959 m, corresponding to the levels of MLM, LLM, and VLLM, respectively. The mesocyclone center is identified by minimum p' and is labeled "M" while the tornado center location is labeled "T". Fig. 9 presents east-west vertical cross sections of w and ζ. Because of the vertical tilt of the vortex, the cross sections are constructed to tilt with height, so that the p'_{min} associated with the vortex center at all levels stays within and at the center of the cross section. In another word, the vertical cross sections follow the vortex central axes with height. This approach was also used by Roberts et al. (2020).

At 6315 s, the mesocyclones at different levels are located within 1.5 km from the tornado location (first column of Fig. 8). At 959 m AGL (Fig. 8m), a small downdraft core is surrounded by a ring of strong positive, with w exceeding 20 m s^{-1}. Higher up, the strongest updraft is located on the west or north side of the mesocyclone center, while weaker negative w exists on the southeast and south side of the mesocyclone center (Fig. 8a and g). In the vertical cross section, positive w is collocated with the

maximum ζ below ~750 m. At higher levels, however, the maximum ζ lies between regions of positive and negative *w* on its west and east sides, respectively (Fig. 9a).

By 6375 s, although the MLM has started to displace northward relative to the tornado (Fig. 8b), the updraft continues to strengthen, particularly below 500 m (Fig. 9b and Fig. 5). The 20 m s^{-1} *w* contours become clearly evident below 500 m by 6425 s (Fig. 9b). Updrafts exceeding 20 m s^{-1} extend downward and upward and reach their greatest intensity at 6525 s (Fig. 9d), coincident with the peak intensity of the surface tornado vortex, which exhibits a solid vorticity core at this time (Fig. 5d). Clearly, between 6315 and 6375 s, the intensifying updrafts below ~750 m and the corresponding near-surface convergence cause the organization and concentration of surface vorticity (see Fig. 5) and intensification of the vortex via enhanced vertical stretching. The continued vertical alignment of the LLM and VLLM during this period (c.f., Fig. 7) likely plays a critical role in maintaining this favorable low-level forcing.

Before 6525 s, in the vertical cross sections, two distinct regions with negative *w* are evident. One region is between ~750 m and 2200 m AGL and is located on the east side of the mesocyclone vortex center (e.g., Fig. 8i, o and Fig. 9b), while updrafts are found on the west side. In horizontal cross sections, this pattern resembles the divided mesocyclone structure described by Lemon and Doswell (1979), in which about one half of the mesocyclone contains positive *w* and the other half contains negative *w*. However, this elevated negative *w* region does not represent sustained downward motion. Later trajectory analysis will show that parcels passing through this region can subsequently ascend rather than descend continuously. Physically, this structure just reflects the mesocyclonic circulation in which generally rising air spirals around the vortex center, with upward motion favored on one side and downward motion on the other. Thus, the downdraft associated with the divided mesocyclone does not necessarily extend to the surface.

Another region with negative *w* occurs below ~750 m AGL and is located near the tornado vortex center (Fig. 8m and Fig. 9a). Although the elevated negative *w* intensifies and gradually descends in height, these two regions remain disconnected both horizontally (Fig. 8m–p) and vertically (Fig. 9a–d) prior to 6525 s. During this period, downdrafts stronger than -8 m s^{-1} are confined to heights above 1000 m (Fig. 9a–d).

After 6525 s, as the VLLM also begins to move northward relative to the tornado (Fig. 8q), the near surface updrafts weaken rapidly, as indicated by the disappearance of the 20 m s^{-1} contour below 500 m (Fig. 9e). The abrupt reduction in updrafts below 500 m is also evident in Fig. 3b and coincides with the onset of tornado weakening. We also note that the 20 m s^{-1} contour below 500 m briefly reappears between 6600 and 6650 s (Fig. 9f), indicating a short-lived reintensification of the updraft below 500 m (see also Fig. 3b). This short-lived recovery will be discussed further in section 4b. Between 6675 and 6750 s, updrafts throughout 500 to 4000 m weaken substantially again (Fig. 9g and h).

As the updrafts below 500 m weakens, downdrafts below 1000 m strengthen considerably after 6525 s (Fig. 8q). In the vertical cross section, it appears that the elevated negative *w* region merges with the central downdraft near the tornado core (Fig. 9e). It then forms a vertically continuous downdraft extending from the surface to approximately 2500 m (Fig. 9f). Therefore, the weakening of updrafts below 500 m, and the intensification of the downdraft near tornado vortex center and its connection with the elevated negative *w* at the mesocyclone levels between 1 and 2.5 km are closely linked to tornado decay. To explain the physical mechanisms responsible for these changes, we next examine the dominant forcing terms in the vertical momentum equation before and after tornado weakening.

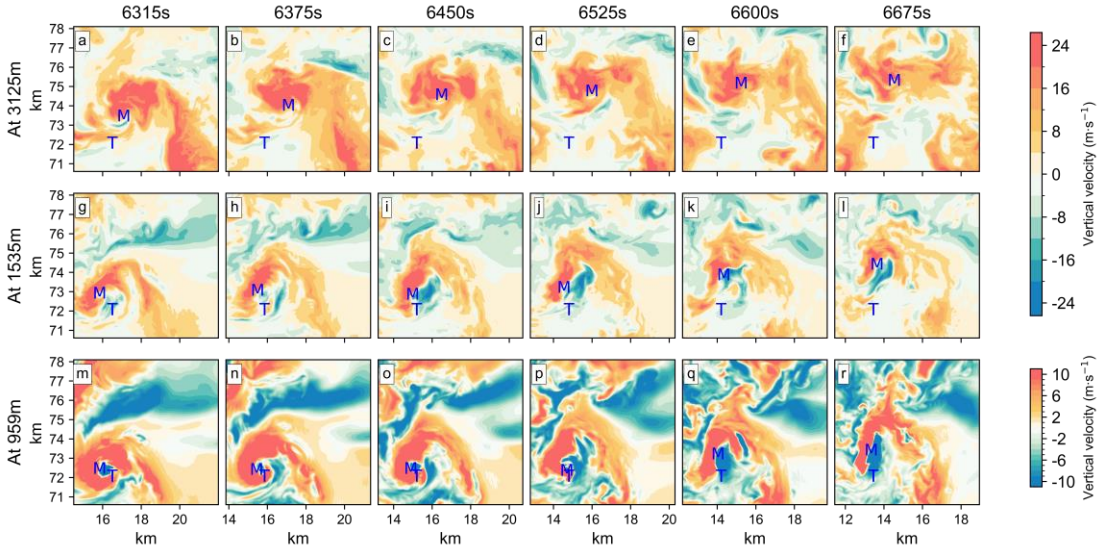


Fig. 8. Horizontal cross sections of *w* (shaded; m s^{-1}) at three levels: (a–f; top row) 3125 m, (g–l; middle row) 1535 m, and (m–r; bottom row) 959 m. Due the smaller magnitude of *w* at 959 m compared to 1535 and 3125 m, a different colormap is used for the 959 m panels. Mesocyclone centers at 1535 (middle

row) and 3125 m (top row), defined by minimum p', are labeled as "M". Tornado center locations are labeled as "T".

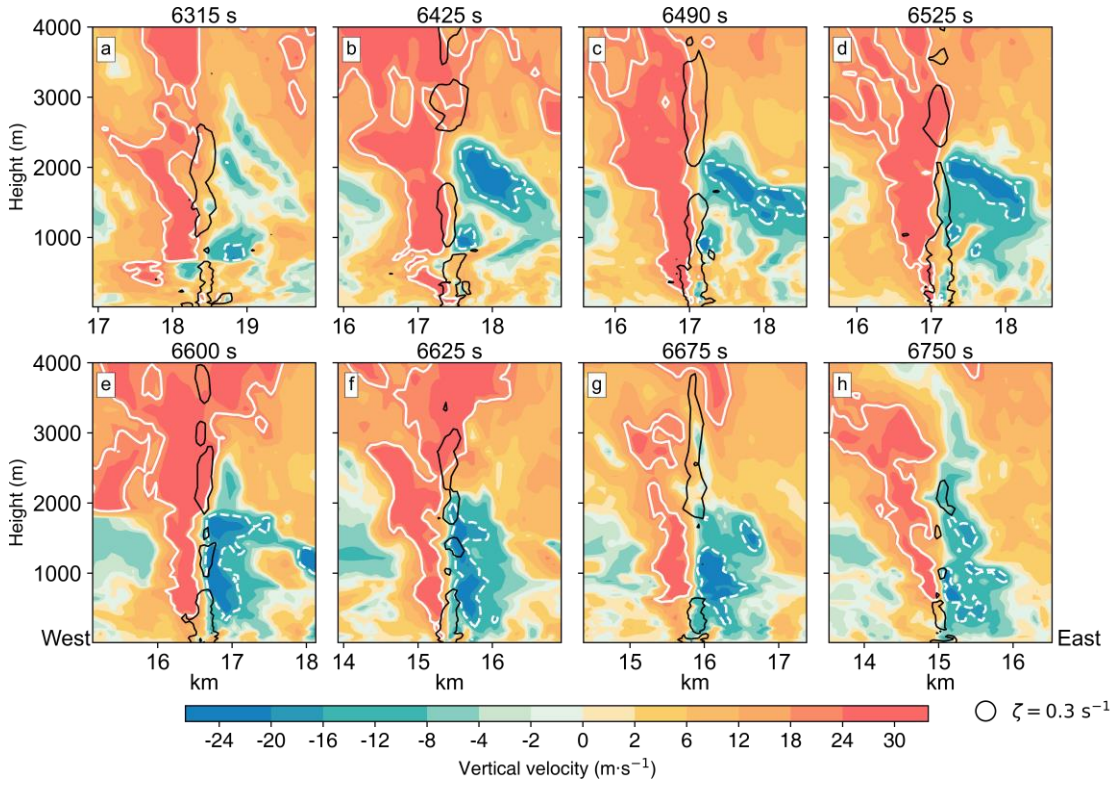


Fig. 9. Vertical cross sections of w (shaded, m s^{-1}; 20 and -15 m s^{-1} contours are in solid and dashed white lines) overlaid with ζ (black contours at 0.18, 0.3 m s^{-1}) at (a) 6315, (b) 6425, (c) 6490, (d) 6525, (e) 6600, (f) 6625, (g) 6675, and (h) 6750 s. Vertical cross-section slopes along the angle of titling vortex tube with increasing height.

b. Diagnostics of vertical accelerations responsible for tornado decay

In previous section, we found that the weakening of updrafts and strengthening of downdrafts associated with the tornado vortex at levels below ~750 m play an important role in tornado decay. In this section, we calculate the individual forcing terms in the w equation to identify the underlying mechanisms.

Neglecting Coriolis effects, the w equation can be written as

$$\frac{dw}{dt} = -\frac{1}{\rho}\frac{\partial p'}{\partial z} + B + F, \qquad (1)$$

where B is buoyancy force and F represents friction and subgrid-scale mixing processes. Term $-\frac{1}{\rho}\frac{\partial p'}{\partial z}$ is the vertical perturbation PGF (VPPGF) and perturbation pressure p' can be decomposed into dynamically induced component p'_d and

buoyancy-induced component p_b' (Davies-Jones 2003; Dawson et al. 2016). With the decomposition, Eq. (1) becomes

$$\frac{dw}{dt} = \underbrace{-\frac{1}{\rho}\frac{\partial p_d'}{\partial z}}_{DVPPGF} \underbrace{-\frac{1}{\rho}\frac{\partial p_b'}{\partial z}}_{BVPPGF} + B + F. \quad (2)$$

$$\underbrace{\qquad\qquad\qquad\qquad}_{EB}$$

The first term on the right-hand side (RHS) is the dynamic VPPGF (DVPPGF). Term $-\frac{1}{\rho}\frac{\partial p_b'}{\partial z}$ is the buoyancy-induced VPPGF (BVPPGF), and the sum of BVPPGF and B is often referred to as effective buoyancy (EB) (Davies-Jones (2003)). BVPPGF often opposes *B*, so using *B* alone may overestimate the net buoyant acceleration. In addition, both *B* and BVPPGF depend on the choice of reference state, whereas EB depends only on horizontal density variations, making EB a more robust diagnostic in convective environments (Davies-Jones 2003; Doswell and Markowski 2004; Dawson et al. 2016; Huang and Xue 2025). The dynamic perturbation pressure p_d' is obtained by solving a diagnostic elliptic equation for $p_d'$where only forcing terms involving velocity components are included. p_b' is obtained as a different between *p*' and p_d'. The same procedure was used in Dawson et al. (2016), Schenkman et al. (2016), and Huang and Xue (2025).

Horizontal cross sections of vertical acceleration (WACCEL) and its components, including DVPPGF and EB, are shown at 1535, 959 and 257 m in Fig. 10, Fig. 11, and Fig. 12, respectively. These levels are located just below MLM, LLM, and VLLM, respectively, and are to represent the vertical accelerations induced by the mesocyclones above. Because the spatial distributions of positive and negative vertical forcing relative to the tornado and mesocyclone centers vary with height and time, it is difficult to use vertical cross sections to illustrate the three-dimensional structure of the forcing fields, we present horizontal cross sections only here. In addition, since the vortex tube is thin and often has significant tilt with height (Fig. 6), vertical acceleration computed as *dw/dz* would show large downward/upward acceleration above/below the vortex axis, distorting the true flow acceleration along the vortex tube axis. To address this, we project the flow acceleration vector onto the local axis of vortex tube, yielding the true acceleration along the vortex tube. For convenience, we still refer to the quantity as "vertical acceleration" in this study.

At all three levels, especially at the 1535, 959 m levels, the spatial patterns of WACCEL (first row of Fig. 10–12) closely resemble those of DVPPGF (second row of Fig. 10–12). This similarity indicates that dynamic forcing is the dominant contributor to the updrafts and downdrafts during the analyzed period. Prior to 6525 s, regions of positive DVPPGF expand at all three levels, indicating strengthening upward dynamic forcing (Fig. 10–12g–i). At 1535 and 959 m, the region of positive DVPPGF exhibits a northeastward extension (Fig. 10 and Fig. 11g–j), which is induced by northward displacement of MLM and LLM shown in Fig. 7. The displacement of MLM and LLM likely also contributes to the expansion of negative DVPPGF. Negative DVPPGF induces the development of a region of elevated negative *w* on the east side of low-level mesocyclone centers (Fig. 9). However, although the area of negative DVPPGF, and thus negative WACCEL, expands somewhat near the mesocyclone center at 1535 m, the area of positive DVPPGF remains larger than that of negative DVPPGF. Thus, despite the displacement of LLM and MLM and the associated expansion of negative DVPPGF beneath them, the dominance of positive DVPPGF allows the updrafts at these levels to continue to intensify before 6525 s.

At 257 m, the area of positive DVPPGF is also larger than that of negative DVPPGF before 6525 s (Fig. 12g–i). The negative and positive DVPPGF regions exhibit an approximate dipole structure, with the positive region occupying a larger area (Fig. 12g–i). Such a dipole structure without evident expansion is consistent with the vertical alignment of the VLLM and surface tornado during this period (Fig. 6 and Fig. 7). Near the mesocyclone center, a small region of negative DVPPGF is present and likely contributes to the downdraft near the vortex center (Fig. 9). This negative DVPPGF should be generated by the stronger near-surface vorticity relative to that aloft, a structure commonly found in mature tornadoes (Huang and Xue 2025). Nevertheless, the dominance of positive DVPPGF at 257 m helps maintain strong near-surface upward acceleration, which is critical for tornado intensification.

The EB also increases before 6525 s, but this increase is mainly obvious at 6450 s at 257 m (Fig. 12o). Because θ' surrounding the tornado is negative at this time (Fig. 4), the contributions to EB from temperature deficit and hydrometeor loading are negative. The increase in EB is from mainly from the pressure drop or negative *p*' (not shown), which causes decrease in air density. This pressure-related component can become large within the tornado vortex (Dawson et al. 2016). Therefore, the enhanced

EB is mainly a consequence, rather than the cause, of tornado intensification. In short, before 6525 s, dynamic forcing provides the primary forcing that strengthens the updrafts (Fig. 9) and supports tornado intensification (Fig. 5).

The role of DVPPGF within the vortex changes abruptly at 6525 s. At this time, a marked weakening in positive DVPPGF and a strengthening of negative DVPPGF near the vortex center are first observed at 257 m (Fig. 12j), coincident with the time when the VLLM also starts to move northward relative to the tornado (Fig. 7). As the VLLM moves away, positive DVPPGF beneath it decreases (Fig. 12j). This decrease leads to weaker WACCEL below 500 m and contributes directly to the weakening of near-surface updraft and intensification of downdraft near the tornado core (Fig. 9e). These changes reduce low-level vertical stretching and are closely associated with the onset of tornado decay after 6525 s (Fig. 5).

The weakening of dynamic forcing is also evident at 959 m and 1535 m (Fig. 10 and Fig. 11). By 6600 s, the regions of positive DVPPGF shrink substantially at both heights (Fig. 10–11k and i), as do the corresponding regions of positive WACCEL (Fig. 10–11e and f). This weakening of DVPPGF explains the reduction of updrafts at these heights shown in Fig. 9. The decrease in EB at 959 and 1535 m is much less evident because EB is considerably weaker at these levels (Fig. 10–11p). These results further support the interpretation that the weakening of DVPPGF is primarily responsible for the weakening of the updrafts during tornado decay.

As noted earlier, a brief recovery of vertical velocity w and ζ, particularly below 500 m, occurs between 6600 and 6650 s (Fig. 3b and Fig. 9e). This recovery is also induced by a temporary reintensification of DVPPGF at 257 m around 6600 s (Fig. 12e). This transient increase in DVPPGF appears to be related to the formation of a secondary LLM directly above the tornado (not shown). This secondary LLM forms from a residual circulation left behind by the primary LLM as it shifts northward and briefly enhances DVPPGF at 959 and 1535 m between 6625 and 6650 s (not shown). Because the secondary LLM is mainly confined between 1000 and 2000 m, the associated DVPPGF enhancement is also largely confined below 2000 m. As the secondary LLM quickly drifts northward relative to the tornado, DVPPGF weakens again and the tornado decay resumes.

In summary, diagnostics of the vertical momentum equation indicate that vertical acceleration is controlled primarily by dynamic perturbation pressure gradient forcing.

Before 6525 s, although the MLM and LLM have shifted northward relative to the tornado, the VLLM and tornado remain vertically aligned. During this period, positive DVPPGF intensifies at all analyzed levels, especially below 500 m, leading to stronger low-level upward acceleration and updraft, and tornado intensification. Though negative DVPPGF also strengthens somewhat above 1000 m in association with the northward displacement of the MLM and LLM, positive DVPPGF remains dominant. The effective buoyancy also increases somewhat at lower levels, but this increase is a result of decreased pressure and associated decrease in air density when the tornado vortex intensifies.

After 6525 s, when the tornado reaches its maximum intensity, the VLLM also begins to shift northward relative to the tornado (Fig. 7). At this time, DVPPGF and therefore WACCEL weakens dramatically below 750 m (Fig. 12j and d). The weakening of dynamic forcing leads to a rapid reduction in updraft intensity below 500 m (Fig. 9), and contributes directly to tornado decay. The weakening of dynamic forcing also explains the weakening of positive WACCEL and updrafts at 959 and 1535 m (Fig. 10–11k).

It is important to emphasize that the spatial patterns of vertical velocity and vertical forcing do not show a strict one to one correspondence (Fig. 10–12). This is because parcel motion depends on time-integrated effects of forcing along trajectories, and because flow within the tornado vortex tube typically follows a spiraling three dimensional path rather than a purely vertical one (see Fig.16 of Huang and Xue 2025). These effects can produce spatial offsets between regions of strongest forcing and regions of largest vertical velocity.

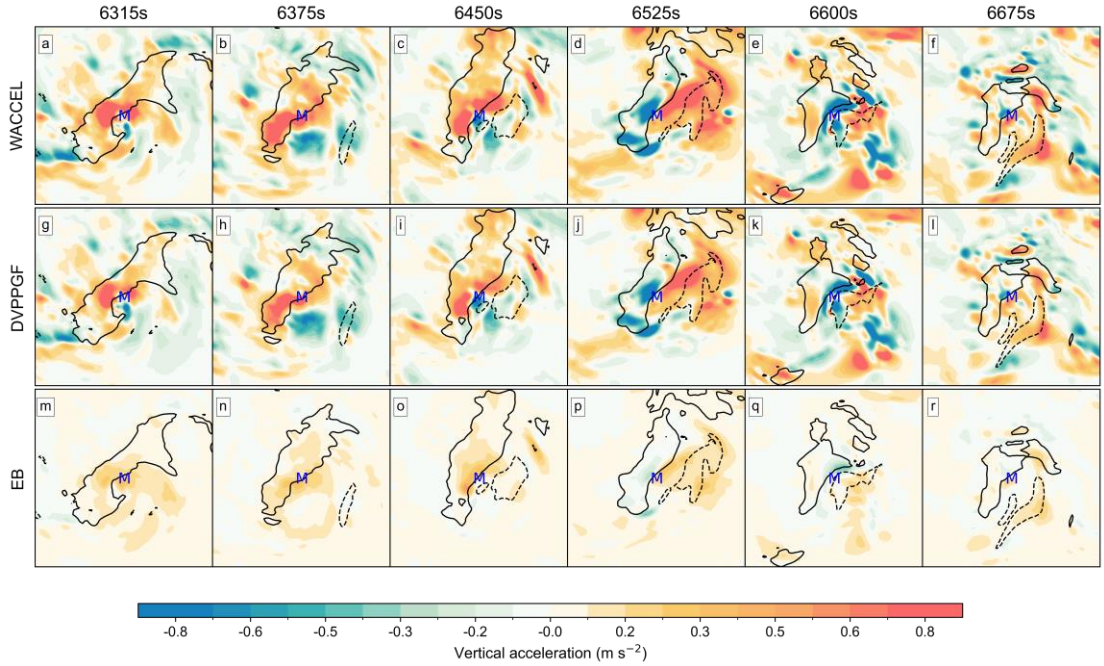


Fig. 10 Horizontal cross sections of (a)–(f) WACCEL, (g)–(l) DVPPGF, and (m)–(r) EB (shaded, m s^{-2}) projected onto the axis of vortex tube overlaid with *w* (contours at -15 and 15 m s^{-1} with negative contours dashed) at 1535 m at (a) 6315, (b) 6375, (c) 6450, (d) 6490, (e) 6525, (f) 6600, (g) 6675, and (h) 6750 s. Mesocyclone center at this level is labeled as "M". The region plotted is 4 × 4 km^2.

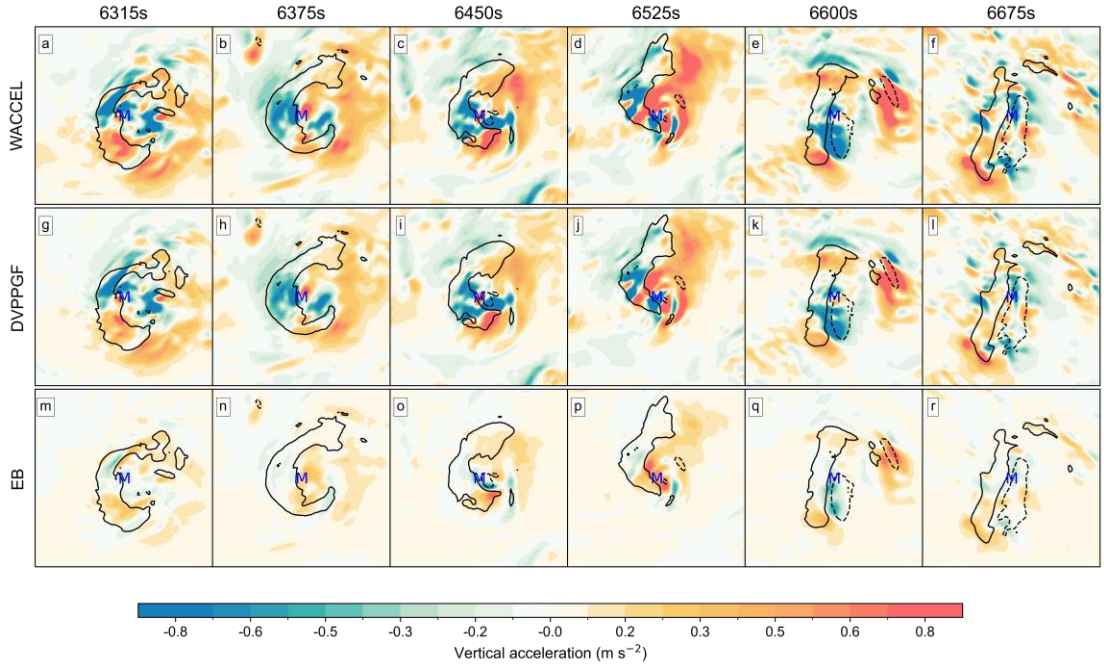


Fig. 11 As in Fig. 10, but for (a)–(f) WACCEL, (g)–(l) DVPPGF, and (m)–(r) EB (shaded, m s^{-2}) overlaid with *w* (contours at -15 and 15 m s^{-1} with negative contours dashed) at 959 m. Mesocyclone center at this level is labeled M. The region plotted is 4 × 4 km^2.

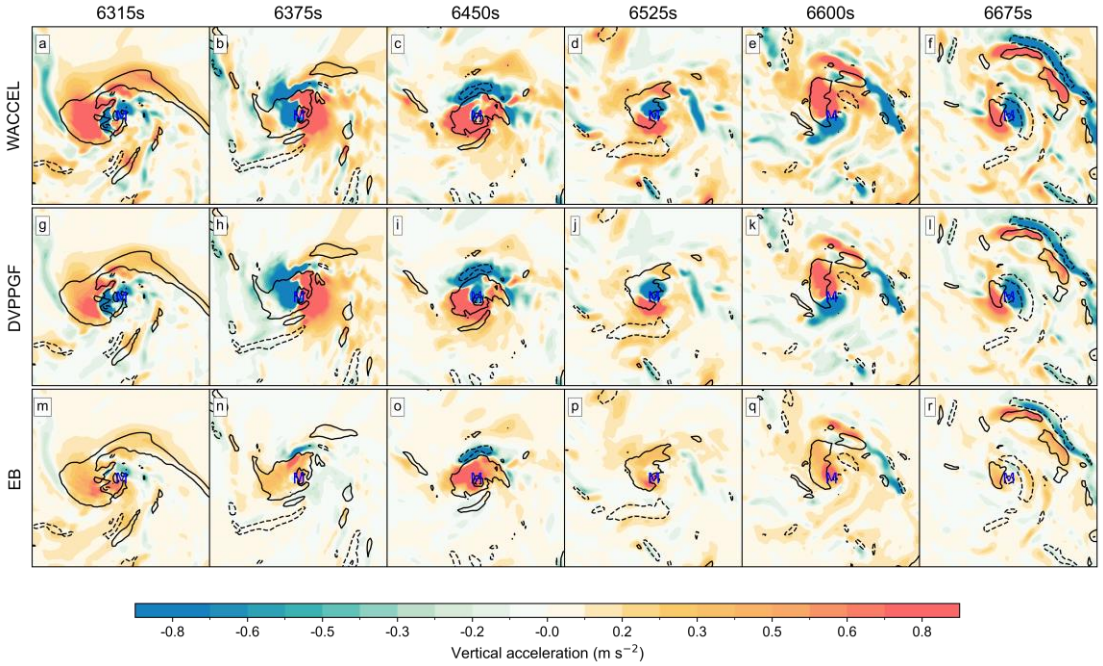


Fig. 12 As in Fig. 10, but for (a)–(f) WACCEL, (g)–(l) DVPPGF, and (m)–(r) EB (shaded, m s^{-2}) overlaid with *w* (contours at -8 and 8 m s^{-1} with negative contours dashed) at 257 m. Mesocyclone center at this level is labeled M. The region plotted is 4 × 4 km^2.

5. Changes in vertical vorticity sources of MLM, LLM, and VLLM during tornado decay

As discussed earlier, the first weakening of the mesocyclone occurs near 2000 m, in the LLM layer, but this does not immediately lead to the weakening of tornado; in fact, the tornado continues to intensify for a short while. Pronounced tornado decay does not begin until the VLLM weakens, apparently as a result of the drifting away of LLM and MLM above. After VLLM weakens, LLM and MLM also start to weaken. Given the critical role of mesocyclones in providing dynamic forcing and vertical stretching to support tornado, this section examines the budgets of vertical vorticity associated with the MLM, LLM, and VLLM in the Eulerian framework first then by tracking Lagrangian parcel trajectories before and after tornado decay. These analyses help explain how mesocyclones at different levels interact with each other and with the tornado.

a. Vertical vorticity budget in the Eulerian framework

The source terms of ζ equation is first examined at 959, 1535, and 3125 m (Fig. 13–15) as for vertical momentum budgets in Fig. 8, roughly corresponding to the levels of VLLM, LLM, and MLM. The ζ equation is

$$\frac{\partial \zeta}{\partial t} = -\nabla \cdot (\boldsymbol{V}_h \zeta) - \frac{\partial w\zeta}{\partial z} + \boldsymbol{\omega_h} \cdot \nabla_h w + \zeta \frac{\partial w}{\partial z} + \frac{1}{\rho^2}\left(\frac{\partial \rho}{\partial x}\frac{\partial p}{\partial y} - \frac{\partial \rho}{\partial y}\frac{\partial p}{\partial x}\right) + \left(\frac{\partial F_y}{\partial x} - \frac{\partial F_x}{\partial y}\right). \quad (3)$$

The RHS terms are the horizontal and vertical advection terms in flux form, tilting of horizontal vorticity $\boldsymbol{\omega}_h$, vertical stretching of ζ, solenoidal generation term, and generation due to horizontal gradient of frictional stress. The Coriolis force is neglected at the tornado scale.

Among the RHS terms, horizontal advection is at least an order of magnitude larger than other terms because of large horizontal wind speed and horizontal gradient of ζ. However, because horizontal advection only moves vorticity around without creating or destroying it, it is not a true vorticity source term. In fact, in a Lagrangian framework, the advection term disappears. Both the solenoidal and frictional terms are much smaller than other terms and are therefore not shown. We will therefore focus on the vertical advection (first rows of Fig. 13–15), vertical stretching (second rows), and tilting terms (third rows).

During the analysis period, vertical advection of ζ is in a general much larger contributor to vorticity changes in the MLM, LLM and VLLM (first rows of Fig. 13–15). The vertical stretching is much smaller, especially at the MLM and LLM levels, due to relatively smaller vertical gradients of *w* at these levels (second rows of Fig. 13–14). The tilting term is small at the MLM and LLM levels (third rows of Fig. 13–14), but it is larger at the VLLM level, especially at 6450 s (Fig. 15o), owing to the presence of larger horizontal vorticity at lower levels.

Between 6315 and 6450 s, vertical advection plays a key role in enhancing ζ at all three levels shown (Fig. 13–15a–c). The extent and magnitude of positive vertical advection are notably greater that those of negative vertical advection. This relatively large vertical advection occurs because, at this stage, the maximum ζ is located near the ground, where it is produced primarily by intense low-level vertical stretching (not shown). The stronger near-surface ζ can then be advected upward by updrafts, thereby supporting the mesocyclones aloft.

After 6525 s, vertical advection of ζ decreases at the three analyzed levels (Fig. 13–15e, f). This decrease is induced by substantial weakening of the updraft below 500 m (Fig. 9), which limits the upward advection of large near-surface ζ. These results highlight that the supply of large vertical vorticity from near the ground is an important process for maintaining mesocyclones at different levels.

As discussed above, the weakening of the updraft below 500 m results primarily from the enhancement of negative DVPPGF at very low levels (Fig. 12), resulting from the northward displacement of the VLLM (Fig. 7). Thus, the northward movement of VLLM on one hand weakens/removes the dynamic-PGF support from above, while at the same time also deprives the mesocyclones themselves of the upward supply of large vertical vorticity from below. Continuous vertical advection of ζ requires the mesocyclones, especially those below 1000 m, to remain connected with the near-surface tornado vortex. This connection is required to maintain strong updrafts that rise from near the ground through the mesocyclones and reach at least the mid-levels.

Additional diagnostics of ζ are conducted at other levels. The results show that above 200 m, vertical advection is the dominant term, whereas below 200 m, vertical stretching is dominant because the vertical gradient of *w* is much larger near the surface. This is consistent with the observational study of Dowell and Bluestein (2002b), which also found that the contribution from vertical advection increases with height while vertical stretching dominates near the surface.

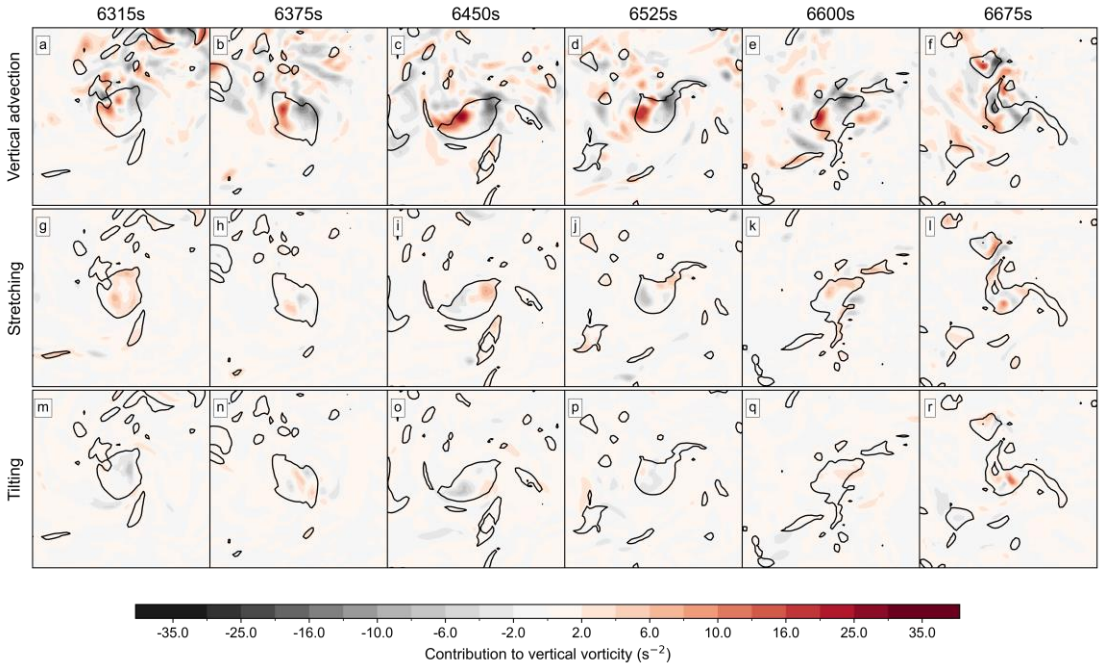


Fig. 13. Vertical vorticity ζ contours at 0.8 s^{-1} and its production terms (shaded, s^{-2}) at ~3125 m AGL, including (a–f) vertical advection, (g–l) vertical stretching, and (m–r) tilting terms at the time shown. For clarity, each term is multiplied by 1000.

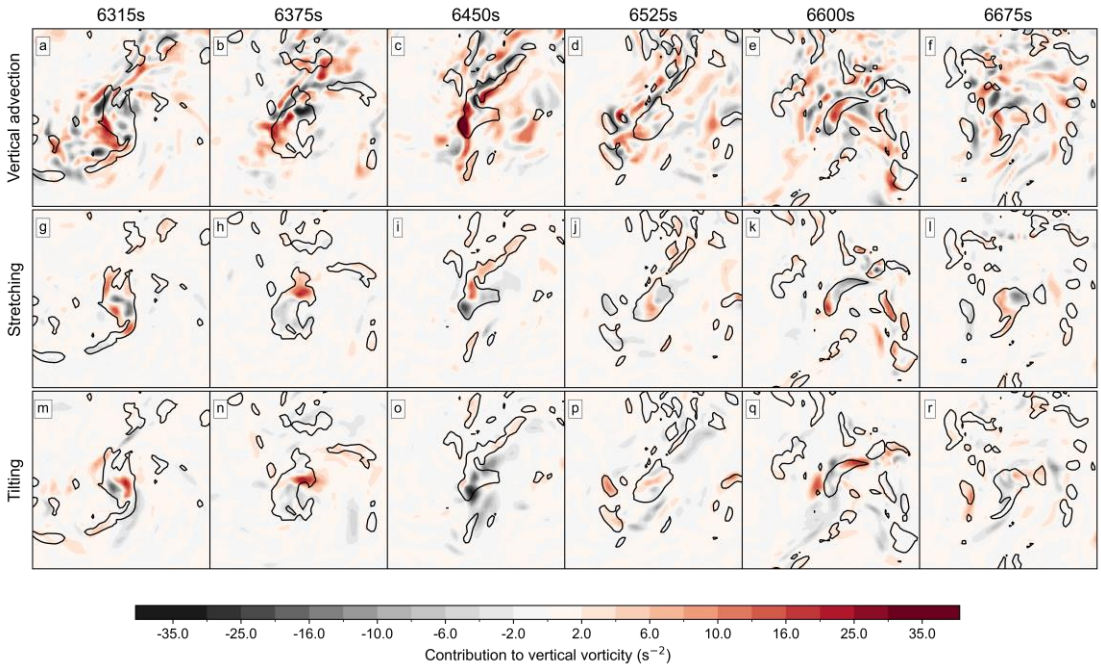


Fig. 14 As in Fig. 13, but for ζ contours at 0.8 s^{-1} and its production terms (shaded, s^{-2}) at 1535 m AGL.

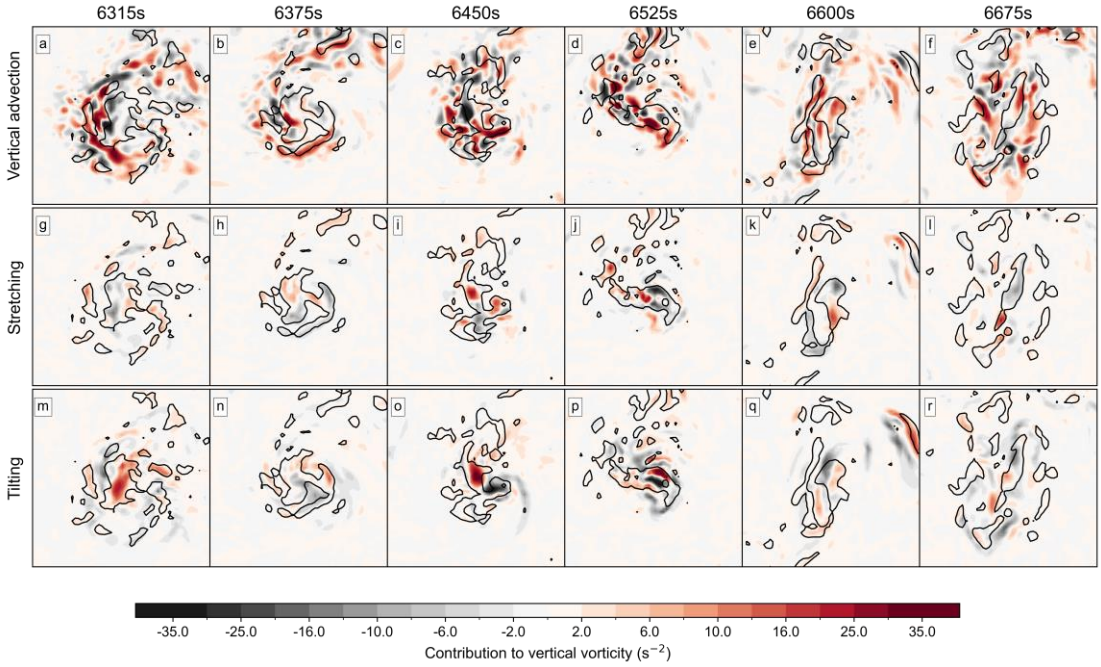


Fig. 15 As in Fig. 13, but for ζ contours at 0.8 s^{-1} and its production terms (shaded, s^{-2}) at 959 m AGL.

b. Trajectory analysis of parcels entering the very low-level mesocyclone

The Eulerian analyses in the previous section indicate that the upward advection of ζ from lower levels is important for the intensification and maintenance of VLLM, LLM and MLM. In this section, we conduct Lagrangian trajectory analyses to further substantiate the findings. Given that the tornado decay occurs as the VLLM moves northward and becomes detached from the tornado, parcels are initialized within a 1.5 × 1.5 km^2 box centered on VLLM at 959 m, with a total of 961 parcels. Forward and backward trajectories are computed for initialization times ranging from 6425 to 6605 s. All trajectories are integrated forward to 7200 s and backward to 5500 s. Fig. 16 shows the time evolution of parcel-height distributions as heat maps. To better illustrate the parcel pathways, two- and three-dimension trajectories are also given in Fig. 17 and Fig. 18, respectively. The trajectory shown are initialized at 6425 (Fig. 17a–c and Fig. 18a–b) and 6625 s (Fig. 17d–f and Fig. 18c–d), corresponding to the times before and after the beginning of tornado decay, respectively. Only parcels with $\zeta > 0.15\ s^{-1}$ at the initialization time are shown in Fig. 17 and Fig. 18. This criterion is satisfied by 77 and 54 parcels initialized at 6425 and 6605 s, respectively.

For trajectories initialized before 6525 s, most parcels share a common behavior: they are located close to the surface just before the initialization time. A smaller fraction of parcels originates somewhat above ground (250-500 m AGL) and then descends toward the surface, while a larger fraction of parcels originates from the near-surface layer (first row of Fig. 16 and Fig. 17a–c). Such behaviors can also be seen more clearly in the 3D trajectory animations provided as supplementary materials, for initialization time of 6425 s.

Just before being ingested into the tornado, most parcels initialized before 6525 s originate from the inflow region east of the tornado; they are not immediately drawn into the tornado from the northern side on their way towards the tornado convergence center. Instead, they turn leftward to go south then enter the tornado from the south (Fig. 17b). At this time, because the VLLM and tornado are vertically aligned (Fig. 7), the dynamic forcing (Fig. 12) and associated updrafts (Fig. 9) are strong. The parcels can then spiral upward within the vortex tube and reach 959 m AGL and beyond (Fig. 17a, c, Fig. 18a–c, and see the animations in supplementary materials). On their way up, the parcels carry larger near-surface ζ upward, helping maintain the VLLM.

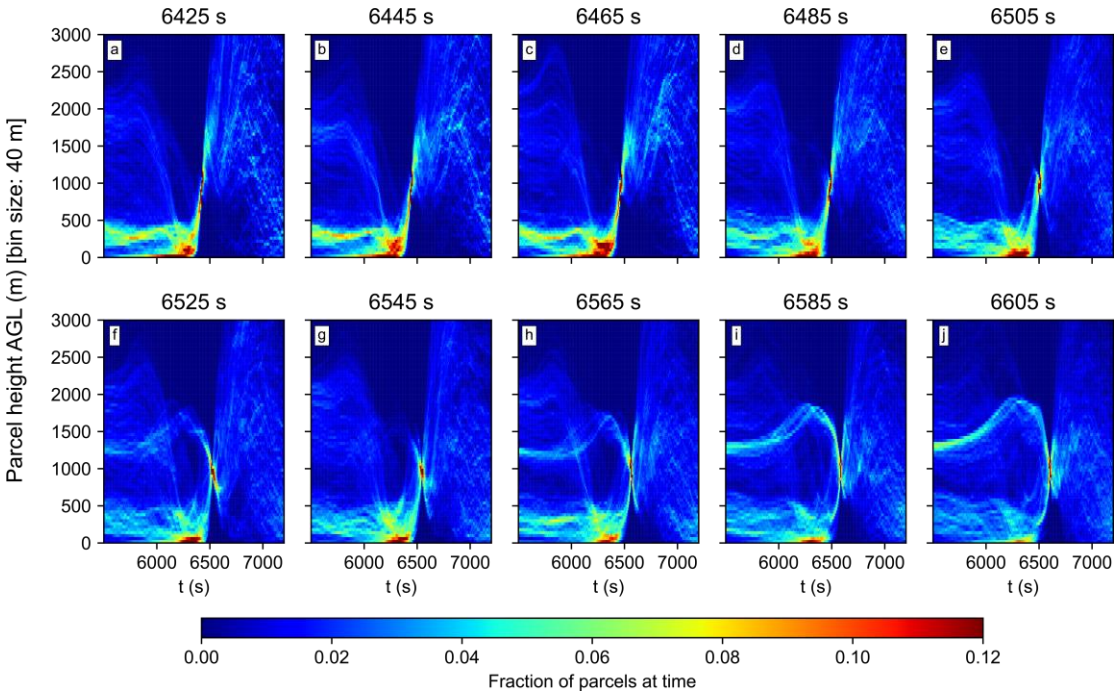


Fig. 16. Heat map of parcel height distribution from 5500 to 7200 s for the parcels initialized at 959 m for different initialization time from 6425 to 6605 s with interval of 20 s. The initialization time is labeled at the top of each panel. The bins are 10 s along the abscissa and 40 m along the ordinate. In each bin, the shading represents the fraction of all parcels at that time shown in abscissa that lie within the height bin.

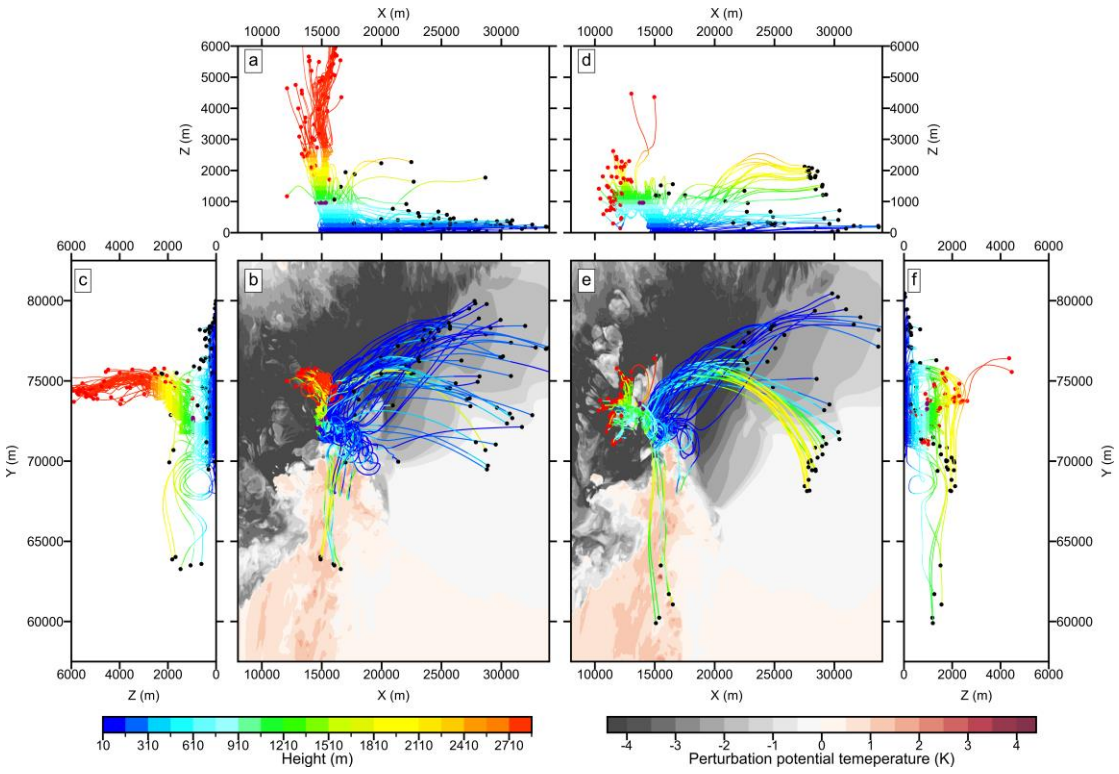


Fig. 17. Trajectories of parcels that pass through mesocyclone center region at 959 m level, initialized at (b) 6425 s and (e) at 6605 s, traced backward to 5500 s and forward for 300 s to 6725 and 6905 s, respectively. Black and red dots mark the initial and final positions of the trajectories, respectively, and the heights of the trajectories are color coded. The θ' at the surface (shaded, K) is also shown. The trajectories are projected onto the side walls in panels (a), (c), (d), and (f). Only parcels with $\zeta > 0.15$ s^{-1} at the initialization time are shown.

After 6525 s, however, the fraction of parcels located near the surface shortly before the initialization time decreases dramatically (second row of Fig. 16 and supplementary materials). Additionally, a larger fraction of the parcels located near the surface shortly before initialization fail to ascend substantially during the following 300 s and remain mostly below 2.5 km AGL (Fig. 17d, f and Fig. 18d–f). These changes indicate that the ability of parcels to carry larger near-surface ζ upward is weakened; in other words, vertical advection of ζ decreases (Fig. 15). Two factors may explain such a change. First, as the updraft weakens below 500 m, fewer parcels are able to rise quickly from the surface. Second, as the elevated negative w on the east side of the mesocyclone intensifies and connects with the lower-level downdraft at tornado core to form a strong downdraft, more elevated parcels are drawn into the tornado vortex from the 1 – 2 km levels (the second row of Fig. 16 and Fig. 17e), and many of these parcels originate from the southern side of the tornado (Fig. 17d–f). The behaviors of these parcels also clearly indicate the change from updraft domination to downdraft domination near tornado core through the decay phase.

We also calculated backward trajectories initialized within the LLM at 1535 m AGL and the MLM at 3125 m AGL (not shown). The results similarly indicate that, before 6525 s, most parcels are first absorbed into the tornado near the surface and then spiral upward quickly into the mesocyclones. For trajectories initialized after 6525 s, however, the fraction of parcels that first descend to the surface and are then drawn into the tornado before rising to the mesocyclones decreases substantially. A larger number of parcels originate from higher levels and enter the mesocyclones from the south side.

These Lagrangian trajectory-based analyses, together with the diagnostics of the ζ budget for the VLLM, LLM, and MLM in a Eulerian framework, collectively demonstrate that during the intensification and maintenance stages of tornado, parcels feeding the VLLM primarily originate from the inflow region east of tornado. These parcels move westward, descending somewhat as they approach the tornadic region

945 before being drawn into the tornado, mostly on the south side. Once absorbed by the
946 convergent flows of the tornado, the parcels will spiral upwards quickly and carry large
947 near-surface ζ generated and intensified by tilting and vertical stretching to higher
948 levels. This upward advection of larger ζ helps sustain the rotation of VLLM, LLM,
949 and MLM.

950 After the time of peak tornado intensity, the fraction of parcels that descend to the
951 surface and are then drawn into the tornado decreases. This change is consistent with
952 the weakening of the updraft and the strengthening of downdrafts below 500 m
953 following the northward movement of mesocyclones (see Fig. 9f–h). These dynamical
954 changes weaken the upward transport of high ζ from near the surface and therefore
955 weaken the mesocyclones. The weakened mesocyclones further decrease vertical
956 velocity and associated vertical stretching, leading to the weakening of tornado.

957 A similar change in parcel-origin height was also noted by Marquis et al. (2016),
958 who conducted trajectory analysis focused on MLM at 5000 m. In their study, during
959 the early development and intensification of tornado, some parcels reaching MLM are
960 found to ascend directly from LLM. However, during the later mature and weakening
961 phases, none of the parcels passing through MLM originates from LLM. Instead,
962 parcels entering MLM originates exclusively from the low-level environmental inflow
963 and are lifted within the low-level updraft that is horizontally displaced from the
964 tornado. In other words, at this stage, the MLM reverts its support from the
965 environmental inflow, rather than by flows passing through the near-surface tornado
966 vortex. This disconnection between the MLM and tornado leads to tornado demise, as
967 we observe in our simulation.

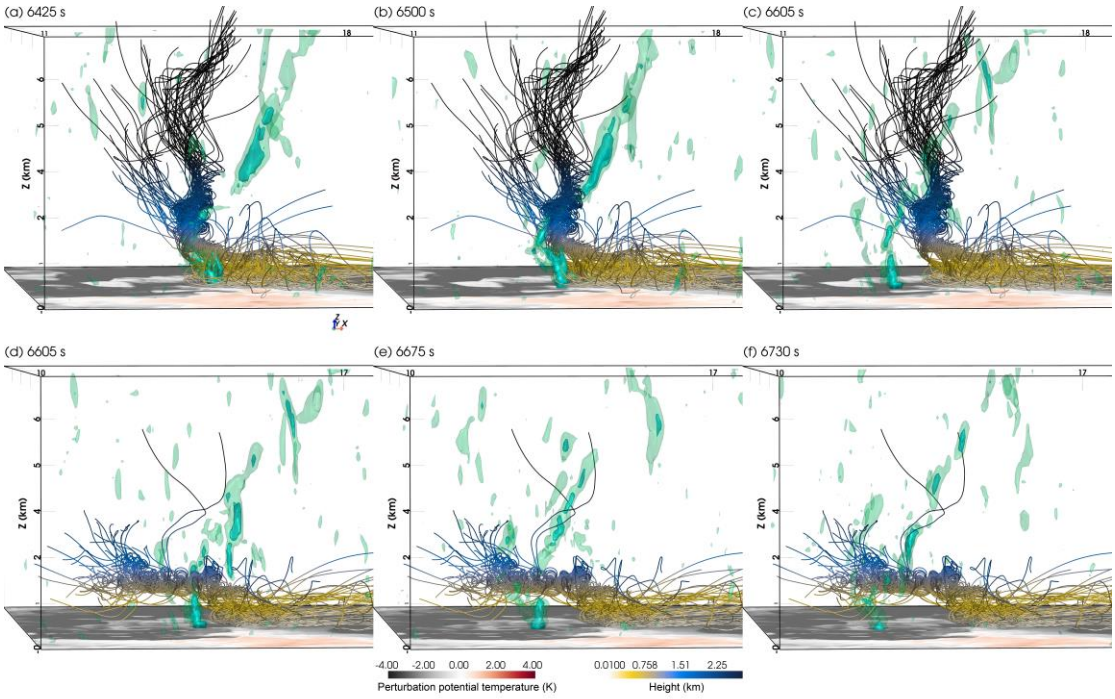


Fig. 18. Three-dimensional air parcel trajectories initialized at (a–c) 6425 s and (c–f) at 6605 s, and traced backward to 5500 s and forward for 300 s to 6725 and 6905 s, respectively. The heights of the trajectories are color coded. The trajectories are viewed from the south. To illustrate the positions of trajectories relative to mesocyclones and surface tornado at different stages, panels (a–c) also show three-dimensional isosurfaces of ζ (0.18, 0.3, 0.4 s^{-1}) with surface θ' (shaded, K) at (a) 6425, (b) 6500, (c) 6605 s for the trajectories initialized at 6425 s and (d) 6605, (e) 6675, (f) 6730 s for the trajectories initialized at 6605 s. Only parcels with $\zeta > 0.15$ s^{-1} at the initialization time are shown.

6. Summary and discussions

In this study, the ARPS model is used to produce an idealized simulation of supercell tornadoes with the inclusion of surface friction. Four tornados are generated in sequence in the simulation. Focusing on the strongest third tornado, we investigate its weakening and decay processes at its final stage. Tornado decay has received much less attention in previous studies than tornadogenesis but is important to the overall tornado life cycle.

Our results show that at 6300 s of simulation, or 225 s before the time of peak tornado intensity at 6525 s, the tornado exhibits a multiple sub-vortex structure. The multiple sub-vortices subsequently converge toward a smaller radius and the tornado evolves into a symmetric one-cell structure with the ζ_{max} located at the tornado center.

After 6525 s, the tornado transitions into a structure of maximum vorticity ring and begins to weaken, with a brief reintensification of surface ζ before the final demise.

Previous studies have proposed that a strong low-level mesocyclone at about 1000 m is important for tornadogenesis which provides strong vertical stretching (Coffer et al. 2017, 2023). In our case, however, the very low-level mesocyclone (VLLM; between 750 and 1000 m) is found to be more directly associated with tornado decay. As the VLLM moves northward following the upper-level mesocyclones and detaches from the tornado at ~6520 s, positive and negative dynamic VPPGF beneath VLLM weakens and intensifies, respectively, strengthening downdrafts and weakening updrafts below 500 m. The weakened updrafts reduce near-surface vertical stretching, thereby contributing to tornado decay. These results suggest that vertical alignment between the VLLM and the tornado is critical for tornado intensification and maintenance.

Maintaining a strong VLLM vertically aligned with the tornado vortex requires sufficiently strong and well-aligned rotational circulations aloft. In our simulation, the northward vortex displacement begins in the mesocyclones aloft and progresses downward through successively lower levels. The first northward displacement occurs above 3000 m, where the mid-level mesocyclone (MLM; 3000–5000 m) resides. As the MLM becomes separated from its lower portion, the positive DVPPGF and associated updraft beneath it shift northward. This displacement subsequently causes the low-level mesocyclone (LLM; 1000–3000 m) to shift northward also relative to the tornado. Finally, at approximately 6520 s, the VLLM also starts to move away from the tornado, tornado decay begins shortly after. In the observational study of Bluestein et al. (2026), it was observed that vortex tilt was minimized when TVS intensity peaked, and vortex tilt increased as the TVS weakened, eventually reversed its direction during TVS dissipation. Such a relation between TVS strength and vortex tilt further suggests that vertical alignment between the tornado and mesocyclones is important for tornado intensification and maintenance.

The northward movement of VLLM on one hand weakens/removes the dynamic-PGF support from above, while at the same time also deprives the mesocyclones themselves of the supply of large vertical vorticity from below. Trajectory analyses, together with Eulerian diagnostics of the ζ budget for the VLLM, LLM, and MLM, show that upward vertical advection of surface ζ plays a critical role in intensifying and

sustaining mesocyclones. When the VLLM and tornado are vertically aligned during tornado intensification, most parcels that enter the VLLM are located near the surface shortly before ascending, and the parcels either originate in the near-surface layer or descend first towards the surface first (see conceptual model in Fig. 19a). Strong updrafts subsequently lift these parcels, carrying with them large near-surface ζ upward and thereby help maintain strong mesocyclones aloft.

After the VLLM detaches from the tornado, the weakening of the updraft below 500 m sharply reduce the fraction of parcels entering the VLLM from near the surface. Instead, a larger number of parcels originate from higher levels and enter the VLLM and higher mesocyclones without passing through the near-surface tornado (Fig. 19b). Even among parcels that pass near the surface, the fraction subsequently lifted above 1 km decreases substantially. The resulting reductions in the vertical advection of large ζ and in vertical stretching directly cause the VLLM weakening and, ultimately, tornado decay. To our knowledge, Dowell and Bluestein (2002b) is the only previous study to note the contribution from the vertical advection of ζ to mesocyclone maintenance. In our study, we also notice a forward surge of a secondary rear-flank gust front (SRFGF) concurrent with tornado decay. Previous works have found that as the cold air behind SRFGF/RFGF wraps around the tornado, tornado starts to weaken. Therefore, they attributed tornado decay to enhanced negatively buoyant forcing in the rear flank downdrafts region. In our simulation, effective buoyancy (EB) also decreases substantially below 500 m after the time of maximum tornado intensity. However, this decrease mainly reflects the weakening of the pressure perturbation deficit near the vortex core and the associated reduction in the perturbation pressure component of EB, rather than being an independent forcing for tornado decay. Thus, EB is not the dominant driver of tornado decay in our case. Instead, the weakening of dynamic forcing associated with the northward displacement of the mesocyclones is primarily responsible for the weakening of the updrafts and subsequent tornado decay.

In our simulation, though the pattern of elevated negative *w* region on the east side of the mesocyclone, which is induced by negative DVPPGF there, resembles the "occlusion downdraft" described by Klemp and Rotunno (1983), they are two separate features until the later stage of tornado decay, when the elevated negative *w* region descends and connects with the low-level occlusion downdraft. The animation of three-dimensional trajectories initialized before the time of maximum tornado intensity

clearly show that before the tornado decay, the elevated negative *w* region simply reflects the downward portion of the spiral motion around the vortex center due to the effect of downward DVPPGF there, it is not truly a region of continuous downward motion. Forward trajectories initialized within the elevated negative *w* region between 1500 and 2500 m before the time of tornado peak intensity (not shown) further show that most parcels actually ascend to higher levels after passing through this negative *w* region rather than continuing downward. The downward and upward spiraling motions on the two sides of the mesocyclone vortex give rise to the well-known "divided mesocyclone" structure (Doswell and Lemon 1979). This structure does not necessarily indicate a dynamically separated mesocyclone; instead, it is simply a result of the overall ascending, spiraling flow within the tornado-mesocyclone vortex. When the tornado–mesocyclone vortex is deep and strong, parcels within the spiraling flow ascend rapidly; as the vortex weakens, however, their overall ascent slows. As discussed below, during the decay stage, the net vertical motion of the spiraling flow may become downward, allowing downdrafts to dominate over updrafts and contributing to tornado demise.

A vertically continuous downdraft from surface to 2.5 km east side of vortex tube, produced by the merger of the elevated negative *w* region and the downdraft near the tornado core, is also observed in our simulation during the tornado decay stage. This downdraft is more consistent with the occlusion downdraft described by Klemp and Rotunno (1983) and Adlerman et al. (1999). Previous studies on tornado weakening have generally suggested that tornado decay occurs when the occlusion downdraft cuts off conditionally unstable inflow feeding the storm updraft (Adlerman et al. 1999). In their study, parcels feeding the mesocyclone were more directly lifted from the inflow region east of the tornado, therefore an occlusion downdraft could effectively disrupt the pathway of the parcels. In our simulation, however, most parcels entering the mesocyclones during tornado intensification are not lifted directly from the inflow region east of the tornado. Instead, they spiral around the tornado vortex and eventually enter the tornado from the southern side mostly. As the strong, vertically continuous downdraft develops, fewer parcels are lifted from near the surface into the mesocyclones, reducing the upward advection of large near-surface ζ. Thus, in our simulation, the low-level occlusion-like downdraft contributes to tornado decay mainly by weakening the upward transport of ζ (as well as weakening the vertical vorticity

stretching) rather than by blocking inflow into the storm updraft. The development of the deep connected downdrafts does help to further separate the low-level tornado vortex from the mid-level mesocyclone that is moving away. As the MLM becomes fed directly by rising inflow air, rather than by the air ascending from below through the tornado-LLM vortex tube, the old tornado dies, while a new, cyclic tornado may develop again.

We note here that some of trajectories from the inflow region in Adlerman et al. (1999) do not feed directly into the mesocyclone either. Instead, they turn leftward, move southward, and enter the mesocyclone from near the surface. These parcels may similarly advect larger near-surface ζ upward, resembling the pathway identified in our simulation. However, Adlerman et al. (1999) did not present three-dimensional trajectory analyses, which is mainly our interpretation. In addition, the coarser horizontal grid spacing of approximately 500 m used by Adlerman et al. (1999) may influence trajectory behavior within strongly convergent tornadic flow. Finally, point out that the conclusions in this paper are only based on the analyses of one decaying tornado in one simulation, additional studies are required to determine the generality of these findings. Analyzing the decaying processes of the other three tornadoes in our simulation is also worthwhile.

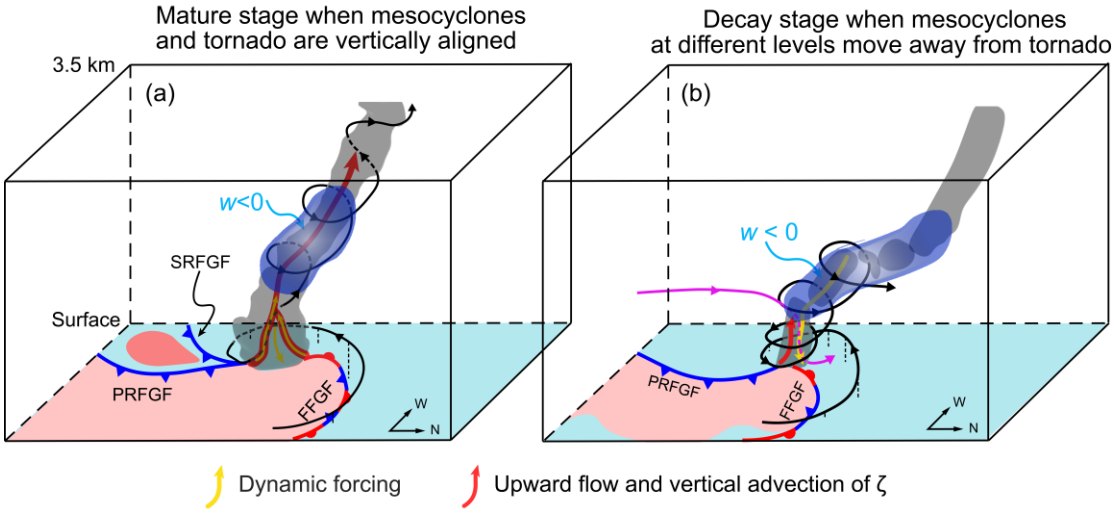


Fig. 19. A conceptual model illustrating the key features at the (a) mature and (b) decay stages of a supercell tornado, including the mesocyclones at different levels, dynamic pressure gradient forcing, the representative upward and downward trajectories through tornado vortex, and surface features. Warm (red) and cold (blue) shading at the surface indicate positive and negative potential temperature perturbations, respectively. Curves with front symbols indicate the positions of the primary rear-flank gust front (PRFGF), primary rear-flank gust front (SRFGF), and forward-flank gust front (FFGF). The warm

anomaly behind PRFGF in (a) is associated with warm surges associated with dynamically forced warm downdrafts. Translucent gray three-dimensional isosurfaces indicate the vortex tubes of the tornado and mesocyclone vortices from surface to ~3.5 km AGL, and translucent light blue regions denote negative *w* associated with mesocyclones. Yellow arrows indicate directions of low-level dynamic forcing, and thick red arrows denote upward flows and associated vertical advection of ζ. (a) At the mature stage of tornado, the mesocyclones and tornado are vertically aligned with only small tilt. A representative inflow trajectory that enters the tornado and mesocyclones is shown by the black arrowed curve. Upward dynamic forcing and the associated updrafts are strong. The elevated negative *w* region as part of the mesocyclone circulations (due to downward tilt of the spiraling circulation) and the downdraft near the tornado core are separated from each other. Most tornado parcels can spiral rapidly upward through the deep, strong tornado–mesocyclone vortex. These parcels originate primarily within the inflow region south of the FFGF and enter the tornado from the south near the surface after curving around on the north and west sides. As these parcels spiral upward from near-surface within the vortex tube, they carry large, near surface vertical vorticity in the tornado upward, helping maintain the mesocyclones (red arrow). The mesocyclones, in turn, provide additional upward dynamic forcing and enhance vertical stretching that intensifies and maintains tornado. (b) During the decay stage, the mesocyclones progressively separate from the surface tornado vortex, beginning at mid-levels and shifting gradually downward to the mesocyclone near 1 km. Representative trajectories entering the mesocyclones are shown by the purple and black arrowed curves. Positive dynamic forcing and the associated updraft (red arrow) weakens, especially below 1 km, as the mid-level mesocyclone becomes disconnected with very-low-level mesocyclone. Meanwhile, the elevated negative *w* region on one side of the midlevel mesocyclone connects downward with the downdraft near the tornado vortex core. Th deeper and strong downdraft along the tornado vortex axis causes expansion and weakening of near-surface tornado vortex. With these changes, more elevated parcels from 1 – 2 km AGL are drawn into the low-level tornado vortex (purple curve), induced by low-level downdrafts. At the same time, the spiraling updraft parcels ascend more slowly along a vertically discontinuous vortex tube and many of them stagnate below 2.5 km and fail to enter the mid-level updraft and mesocyclone. These changes reduce the vertical advection of larger near-surface vertical vorticity and weaken vertical stretching, which directly contribute to mesocyclone weakening and, ultimately, tornado decay.

Acknowledgements.

This work was primarily supported by NSFC grant 42588101. The numerical calculations in this paper have been done on the computing facilities in the High Performance Computing Center (HPCC) of Nanjing University.

Data Availability Statement.

The data used in this paper can be found at Harvard Dataverse at https://dataverse.harvard.edu/dataset.xhtml?persistentId=doi:10.7910/DVN/DUL5WN&version=DRAFT.

References

Adlerman, E. J., and K. K. Droegemeier, 2002: The Sensitivity of Numerically Simulated Cyclic Mesocyclogenesis to Variations in Model Physical and Computational Parameters. *Monthly Weather Review*, **130**, 2671–2691, https://doi.org/10.1175/1520-0493(2002)130%3C2671:TSONSC%3E2.0.CO;2.

——, and ——, 2005: The Dependence of Numerically Simulated Cyclic Mesocyclogenesis upon Environmental Vertical Wind Shear. *Monthly Weather Review*, **133**, 3595–3623, https://doi.org/10.1175/MWR3039.1.

——, ——, and R. Davies-Jones, 1999: A Numerical Simulation of Cyclic Mesocyclogenesis. *Journal of the Atmospheric Sciences*, **56**, 2045–2069, https://doi.org/10.1175/1520-0469(1999)056%3C2045:ANSOCM%3E2.0.CO;2.

Beck, J. R., J. L. Schroeder, and J. M. Wurman, 2006: High-Resolution Dual-Doppler Analyses of the 29 May 2001 Kress, Texas, Cyclic Supercell. *Monthly Weather Review*, **134**, 3125–3148, https://doi.org/10.1175/MWR3246.1.

Bluestein, H. B., K. J. Thiem, J. C. Snyder, and J. B. Houser, 2019: Tornadogenesis and Early Tornado Evolution in the El Reno, Oklahoma, Supercell on 31 May 2013. *Monthly Weather Review*, **147**, 2045–2066, https://doi.org/10.1175/MWR-D-18-0338.1.

——, J. A. Margraf, T. A. Greenwood, S. Emmerson, J. C. Snyder, L. J. Wicker, and D. J. Bodine, 2026: The Evolution of a Cyclonic Tornado in the Selden, Kansas, Supercell of 24 May 2021: Rapid-Scan, Polarimetric, Mobile, X-Band, Doppler Radar Observations. *Monthly Weather Review*, **154**, 137–162, https://doi.org/10.1175/MWR-D-25-0035.1.

Burgess, D. W., V. T. Wood, and R. A. Brown, 1982: Mesocyclone evolution statistics. *12th Conf. on Severe Local Storms*, San Antonio, Amer. Meteor. Soc., 422–424.

Coffer, B. E., M. D. Parker, J. M. L. Dahl, L. J. Wicker, and A. J. Clark, 2017: Volatility of Tornadogenesis: An Ensemble of Simulated Nontornadic and Tornadic Supercells in VORTEX2 Environments. *Monthly Weather Review*, **145**, 4605–4625, https://doi.org/10.1175/MWR-D-17-0152.1.

——, ——, J. M. Peters, and A. R. Wade, 2023: Supercell Low-Level Mesocyclones: Origins of Inflow and Vorticity. *Monthly Weather Review*, **151**, 2205–2232, https://doi.org/10.1175/MWR-D-22-0269.1.

Dahl, J. M. L., 2015: Near-Ground Rotation in Simulated Supercells: On the Robustness of the Baroclinic Mechanism. *Monthly Weather Review*, **143**, 4929–4942, https://doi.org/10.1175/MWR-D-15-0115.1.

——, M. D. Parker, and L. J. Wicker, 2014: Imported and Storm-Generated Near-Ground Vertical Vorticity in a Simulated Supercell. *Journal of the Atmospheric Sciences*, **71**, 3027–3051, https://doi.org/10.1175/JAS-D-13-0123.1.

Davies-Jones, R., 2003: An Expression for Effective Buoyancy in Surroundings with Horizontal Density Gradients. *Journal of the Atmospheric Sciences*, **60**, 2922–2925, https://doi.org/10.1175/1520-0469(2003)060%3C2922:AEFEBI%3E2.0.CO;2.

——, 2008: Can a Descending Rain Curtain in a Supercell Instigate Tornadogenesis Barotropically? *Journal of the Atmospheric Sciences*, **65**, 2469–2497, https://doi.org/10.1175/2007JAS2516.1.

——, and H. Brooks, 1993: Mesocyclogenesis From a Theoretical Perspective. *The Tornado: Its Structure, Dynamics, Prediction, and Hazards*, C. Church, D. Burgess, C. Doswell, and R. Davies-Jones, Eds, Vol. 79 of, American Geophysical Union, 105–114, https://doi.org/10.1029/GM079p0105.

——, R. J. Trapp, and H. B. Bluestein, 2001: Tornadoes and Tornadic Storms. *Severe Convective Storms*, C.A. Doswell, Ed., American Meteorological Society, 167–221, https://doi.org/10.1007/978-1-935704-06-5_5.

Dawson, D. T., M. Xue, J. A. Milbrandt, and M. K. Yau, 2010: Comparison of Evaporation and Cold Pool Development between Single-Moment and Multimoment Bulk Microphysics Schemes in Idealized Simulations of Tornadic Thunderstorms. *Monthly Weather Review*, **138**, 1152–1171, https://doi.org/10.1175/2009MWR2956.1.

——, ——, A. Shapiro, J. A. Milbrandt, and A. D. Schenkman, 2016: Sensitivity of Real-Data Simulations of the 3 May 1999 Oklahoma City Tornadic Supercell and Associated Tornadoes to Multimoment Microphysics. Part II: Analysis of Buoyancy and Dynamic Pressure Forces in Simulated Tornado-Like Vortices. *Journal of the Atmospheric Sciences*, **73**, 1039–1061, https://doi.org/10.1175/JAS-D-15-0114.1.

——, B. Roberts, and M. Xue, 2019: A Method to Control the Environmental Wind Profile in Idealized Simulations of Deep Convection with Surface Friction. *Monthly Weather Review*, **147**, 3935–3954, https://doi.org/10.1175/MWR-D-18-0462.1.

Doswell, C. A., and P. M. Markowski, 2004: Is Buoyancy a Relative Quantity? *Monthly Weather Review*, **132**, 853–863, https://doi.org/10.1175/1520-0493(2004)132%3C0853:IBARQ%3E2.0.CO;2.

Dowell, D. C., and H. B. Bluestein, 2002a: The 8 June 1995 McLean, Texas, Storm. Part I: Observations of Cyclic Tornadogenesis. *Monthly Weather Review*, **130**, 2626–2648, https://doi.org/10.1175/1520-0493(2002)130%3C2626:TJMTSP%3E2.0.CO;2.

——, and ——, 2002b: The 8 June 1995 McLean, Texas, Storm. Part II: Cyclic Tornado Formation, Maintenance, and Dissipation. *Monthly Weather Review*, **130**, 2649–2670, https://doi.org/10.1175/1520-0493(2002)130%3C2649:TJMTSP%3E2.0.CO;2.

Fiedler, B. H., 1998: Wind-Speed Limits in Numerically Simulated Tornadoes with Suction Vortices. *Quarterly Journal of the Royal Meteorological Society*, **124**, 2377–2392, https://doi.org/10.1002/qj.49712455110.

Fischer, J., and J. M. L. Dahl, 2022: Supercell-External Storms and Boundaries Acting as Catalysts for Tornadogenesis. *Monthly Weather Review*, **151**, 23–38, https://doi.org/10.1175/MWR-D-22-0026.1.

French, M. M., H. B. Bluestein, D. C. Dowell, L. J. Wicker, M. R. Kramar, and A. L. Pazmany, 2008: High-Resolution, Mobile Doppler Radar Observations of Cyclic

Mesocyclogenesis in a Supercell. *Monthly Weather Review*, **136**, 4997–5016, https://doi.org/10.1175/2008MWR2407.1.

——, ——, I. PopStefanija, C. A. Baldi, and R. T. Bluth, 2014: Mobile, Phased-Array, Doppler Radar Observations of Tornadoes at X Band. *Monthly Weather Review*, **142**, 1010–1036, https://doi.org/10.1175/MWR-D-13-00101.1.

Fujita, T. T., 1970: The Lubbock Tornadoes: A Study of Suction Spots. *Weatherwise*, **23**, 161–173, https://doi.org/10.1080/00431672.1970.9932888.

Fujita, T. T., 1972: Tornadoes in Japan and New Evidence. *Journal of the Meteorological Society of Japan*, **50**, 23.

Houser, J. L., H. B. Bluestein, and J. C. Snyder, 2015: Rapid-Scan, Polarimetric, Doppler Radar Observations of Tornadogenesis and Tornado Dissipation in a Tornadic Supercell: The "El Reno, Oklahoma" Storm of 24 May 2011. *Monthly Weather Review*, **143**, 2685–2710, https://doi.org/10.1175/MWR-D-14-00253.1.

Huang, W., and M. Xue, 2023: Sub-vortices Within a Numerically Simulated Tornado: The Role of Unstable Vortex Rossby Waves. *Journal of the Atmospheric Sciences*, **1**, https://doi.org/10.1175/JAS-D-22-0237.1.

——, and ——, 2025: What Forces the Rapid Vertical Acceleration and Vorticity Intensification near Ground in Tornadoes? Diagnostic Analysis Based on a Numerically Simulated Real Tornado, https://doi.org/10.1175/JAS-D-25-0033.1.

Klemp, J. B., 1987: Dynamics of Tornadic Thunderstorms. *Annual Review of Fluid Mechanics*, **19**, 369–402, https://doi.org/10.1146/annurev.fl.19.010187.002101.

Klemp, J. B., and R. Rotunno, 1983: A Study of the Tornadic Region within a Supercell Thunderstorm. *Journal of the Atmospheric Sciences*, **40**, 359–377, https://doi.org/10.1175/1520-0469(1983)040%3C0359:ASOTTR%3E2.0.CO;2.

Kosiba, K., and J. Wurman, 2010: The Three-Dimensional Axisymmetric Wind Field Structure of the Spencer, South Dakota, 1998 Tornado. *Journal of the Atmospheric Sciences*, **67**, 3074–3083, https://doi.org/10.1175/2010JAS3416.1.

——, ——, Y. Richardson, P. Markowski, P. Robinson, and J. Marquis, 2013: Genesis of the Goshen County, Wyoming, Tornado on 5 June 2009 during VORTEX2.

Monthly Weather Review, **141**, 1157–1181, https://doi.org/10.1175/MWR-D-12-00056.1.

Lee, B. D., C. A. Finley, and C. D. Karstens, 2012: The Bowdle, South Dakota, Cyclic Tornadic Supercell of 22 May 2010: Surface Analysis of Rear-Flank Downdraft Evolution and Multiple Internal Surges. *Monthly Weather Review*, **140**, 3419–3441, https://doi.org/10.1175/MWR-D-11-00351.1.

Lemon, L. R., and C. A. Doswell, 1979: Severe Thunderstorm Evolution and Mesocyclone Structure as Related to Tornadogenesis. *Monthly Weather Review*, **107**, 1184–1197, https://doi.org/10.1175/1520-0493(1979)107%3C1184:STEAMS%3E2.0.CO;2.

Lewellen, W. S., D. C. Lewellen, and R. I. Sykes, 1997: Large-Eddy Simulation of a Tornado's Interaction with the Surface. *Journal of the Atmospheric Sciences*, **54**, 581–605, https://doi.org/10.1175/1520-0469(1997)054%3C0581:LESOAT%3E2.0.CO;2.

Li, H., and M. Xue, 2026: Improving the Prediction of the 3 July 2019 Kaiyuan Tornadic Supercell and Embedded Tornado with Radar and Surface Data Assimilation. *Qarterly Journal of the Royal Meteorological Society*.

Lin, Y.-L., R. D. Farley, and H. D. Orville, 1983: Bulk Parameterization of the Snow Field in a Cloud Model. *Journal of Applied Meteorology and Climatology*, **22**, 1065–1092, https://doi.org/10.1175/1520-0450(1983)022%3C1065:BPOTSF%3E2.0.CO;2.

Markowski, P. M., 2016: An Idealized Numerical Simulation Investigation of the Effects of Surface Drag on the Development of Near-Surface Vertical Vorticity in Supercell Thunderstorms. *Journal of the Atmospheric Sciences*, **73**, 4349–4385, https://doi.org/10.1175/JAS-D-16-0150.1.

——, 2020: What is the Intrinsic Predictability of Tornadic Supercell Thunderstorms? *Monthly Weather Review*, **148**, 3157–3180, https://doi.org/10.1175/MWR-D-20-0076.1.

——, 2024: A New Pathway for Tornadogenesis Exposed by Numerical Simulations of Supercells in Turbulent Environments. *Journal of the Atmospheric Sciences*, **81**, 481–518, https://doi.org/10.1175/JAS-D-23-0161.1.

——, and Y. P. Richardson, 2014: The Influence of Environmental Low-Level Shear and Cold Pools on Tornadogenesis: Insights from Idealized Simulations. *Journal of the Atmospheric Sciences*, **71**, 243–275, https://doi.org/10.1175/JAS-D-13-0159.1.

Marquis, J., Y. Richardson, P. Markowski, D. Dowell, and J. Wurman, 2012: Tornado Maintenance Investigated with High-Resolution Dual-Doppler and EnKF Analysis. *Monthly Weather Review*, **140**, 3–27, https://doi.org/10.1175/MWR-D-11-00025.1.

——, ——, ——, J. Wurman, K. Kosiba, and P. Robinson, 2016: An Investigation of the Goshen County, Wyoming, Tornadic Supercell of 5 June 2009 Using EnKF Assimilation of Mobile Mesonet and Radar Observations Collected during VORTEX2. Part II: Mesocyclone-Scale Processes Affecting Tornado Formation, Maintenance, and Decay. *Monthly Weather Review*, **144**, 3441–3463, https://doi.org/10.1175/MWR-D-15-0411.1.

Mashiko, W., and H. Niino, 2017: Super High-Resolution Simulation of the 6 May 2012 Tsukuba Supercell Tornado: Near-Surface Structure and Its Evolution. *SOLA*, **13**, 135–139, https://doi.org/10.2151/sola.2017-025.

——, ——, and T. Kato, 2009: Numerical Simulation of Tornadogenesis in an Outer-Rainband Minisupercell of Typhoon Shanshan on 17 September 2006. *Monthly Weather Review*, **137**, 4238–4260, https://doi.org/10.1175/2009MWR2959.1.

Moeng, C.-H., and J. C. Wyngaard, 1988: Spectral Analysis of Large-Eddy Simulations of the Convective Boundary Layer. *Journal of the Atmospheric Sciences*, **45**, 3573–3587, https://doi.org/10.1175/1520-0469(1988)045%3C3573:SAOLES%3E2.0.CO;2.

Nolan, D. S., N. A. Dahl, G. H. Bryan, and R. Rotunno, 2017: Tornado Vortex Structure, Intensity, and Surface Wind Gusts in Large-Eddy Simulations with Fully Developed Turbulence. *Journal of the Atmospheric Sciences*, **74**, 1573–1597, https://doi.org/10.1175/JAS-D-16-0258.1.

Oliveira, M. I., M. Xue, and B. Roberts, 2022: Trailing Horizontal Vortices in Observed and Numerically Simulated Tornadoes. *Bulletin of the American Meteorological Society*, **103**, E2768–E2790, https://doi.org/10.1175/BAMS-D-20-0251.1.

Orf, L., R. Wilhelmson, B. Lee, C. Finley, and A. Houston, 2017: Evolution of a Long-Track Violent Tornado within a Simulated Supercell. *Bulletin of the American Meteorological Society*, **98**, 45–68, https://doi.org/10.1175/BAMS-D-15-00073.1.

Parker, M. D., 2023: How Well Must Surface Vorticity Be Organized for Tornadogenesis? *Journal of the Atmospheric Sciences*, **80**, 1433–1448, https://doi.org/10.1175/JAS-D-22-0195.1.

Peters, J. M., 2016: The Impact of Effective Buoyancy and Dynamic Pressure Forcing on Vertical Velocities within Two-Dimensional Updrafts. *Journal of the Atmospheric Sciences*, **73**, 4531–4551, https://doi.org/10.1175/JAS-D-16-0016.1.

Rasmussen, E. N., and J. M. Straka, 2007: Evolution of Low-Level Angular Momentum in the 2 June 1995 Dimmitt, Texas, Tornado Cyclone. *Journal of the Atmospheric Sciences*, **64**, 1365–1378, https://doi.org/10.1175/JAS3829.1.

Roberts, B., and M. Xue, 2017: The Role of Surface Drag in Mesocyclone Intensification Leading to Tornadogenesis within an Idealized Supercell Simulation. *Journal of the Atmospheric Sciences*, **74**, 3055–3077, https://doi.org/10.1175/JAS-D-16-0364.1.

——, ——, A. D. Schenkman, and D. T. Dawson, 2016: The Role of Surface Drag in Tornadogenesis within an Idealized Supercell Simulation. *Journal of the Atmospheric Sciences*, **73**, 3371–3395, https://doi.org/10.1175/JAS-D-15-0332.1.

——, ——, and D. T. Dawson, 2020: The Effect of Surface Drag Strength on Mesocyclone Intensification and Tornadogenesis in Idealized Supercell Simulations. *Journal of the Atmospheric Sciences*, **77**, 1699–1721, https://doi.org/10.1175/JAS-D-19-0109.1.

Rotunno, R., 1984: An Investigation of a Three-Dimensional Asymmetric Vortex. *Journal of the Atmospheric Sciences*, **41**, 283–298, https://doi.org/10.1175/1520-0469(1984)041%3C0283:AIOATD%3E2.0.CO;2.

——, P. M. Markowski, and G. H. Bryan, 2017: "Near Ground" Vertical Vorticity in Supercell Thunderstorm Models. *Journal of the Atmospheric Sciences*, **74**, 1757–1766, https://doi.org/10.1175/JAS-D-16-0288.1.

Schenkman, A. D., M. Xue, and M. Hu, 2014: Tornadogenesis in a High-Resolution Simulation of the 8 May 2003 Oklahoma City Supercell. *Journal of the Atmospheric Sciences*, **71**, 130–154, https://doi.org/10.1175/JAS-D-13-073.1.

——, ——, and D. T. Dawson II, 2016: The Cause of Internal Outflow Surges in a High-Resolution Simulation of the 8 May 2003 Oklahoma City Tornadic Supercell. *Journal of the Atmospheric Sciences*, **73**, 353–370, https://doi.org/10.1175/JAS-D-15-0112.1.

Skinner, P. S., C. C. Weiss, M. M. French, H. B. Bluestein, P. M. Markowski, and Y. P. Richardson, 2014: VORTEX2 Observations of a Low-Level Mesocyclone with Multiple Internal Rear-Flank Downdraft Momentum Surges in the 18 May 2010 Dumas, Texas, Supercell. *Monthly Weather Review*, **142**, 2935–2960, https://doi.org/10.1175/MWR-D-13-00240.1.

Snook, N., and M. Xue, 2008: Effects of Microphysical Drop Size Distribution on Tornadogenesis in Supercell Thunderstorms. *Geophysical Research Letters*, **35**, L24803, https://doi.org/10.1029/2008GL035866.

Sun, Z., M. Xue, K. Zhu, and B. Zhou, 2019: Prediction of an EF4 Supercell Tornado in Funing, China: Resolution Dependency of Simulated Tornadoes and Their Structures. *Atmospheric Research*, **229**, 175–189, https://doi.org/10.1016/j.atmosres.2019.06.019.

Tao, T., and T. Tamura, 2020: Numerical Study of the 6 May 2012 Tsukuba Supercell Tornado: Vorticity Sources Responsible for Tornadogenesis. *Monthly Weather Review*, **148**, 1205–1228, https://doi.org/10.1175/MWR-D-19-0095.1.

Wurman, J., 2002: The Multiple-Vortex Structure of a Tornado. *Weather and Forecasting*, **17**, 473–505, https://doi.org/10.1175/1520-0434(2002)017%3C0473:TMVSOA%3E2.0.CO;2.

——, K. Kosiba, P. Markowski, Y. Richardson, D. Dowell, and P. Robinson, 2010: Finescale Single- and Dual-Doppler Analysis of Tornado Intensification, Maintenance, and Dissipation in the Orleans, Nebraska, Supercell. *Monthly Weather Review*, **138**, 4439–4455, https://doi.org/10.1175/2010MWR3330.1.

Xu, X., M. Xue, and Y. Wang, 2015: The Genesis of Mesovortices within a Real-Data Simulation of a Bow Echo System. *Journal of the Atmospheric Sciences*, **72**, 1963–1986, https://doi.org/10.1175/JAS-D-14-0209.1.

Xue, M., and Coauthors, 2001: The Advanced Regional Prediction System (ARPS) – A multi-scale nonhydrostatic atmospheric simulation and prediction tool. Part II: Model physics and applications. *Meteorology and Atmospheric Physics*, **76**, 143–165, https://doi.org/10.1007/s007030170027.

Xue, M., M. Hu, and A. D. Schenkman, 2014: Numerical Prediction of the 8 May 2003 Oklahoma City Tornadic Supercell and Embedded Tornado Using ARPS with the Assimilation of WSR-88D Data. *Weather and Forecasting*, **29**, 39–62, https://doi.org/10.1175/WAF-D-13-00029.1.

Yao, D., Z. Meng, and M. Xue, 2019: Genesis, Maintenance and Demise of a Simulated Tornado and the Evolution of Its Preceding Descending Reflectivity Core (DRC). *Atmosphere*, **10**, 236, https://doi.org/10.3390/atmos10050236.

Yokota, S., H. Niino, H. Seko, M. Kunii, and H. Yamauchi, 2018: Important Factors for Tornadogenesis as Revealed by High-Resolution Ensemble Forecasts of the Tsukuba Supercell Tornado of 6 May 2012 in Japan. *Monthly Weather Review*, **146**, 1109–1132, https://doi.org/10.1175/MWR-D-17-0254.1.